



RealBench

Operational Weather Forecasting
Benchmark | arXiv Preprint

RealBench: Benchmarking Data-Driven Numerical Weather Forecasting Under Operational Conditions and Extreme Event Challenges

Ruize Li^{1,2*} Zhibin Wen^{3*} Tao Han^{1,4*†} Hao Chen¹ Fenghua Ling⁴ Wei Zhang⁵
Song Guo^{1§} Lei Bai^{4§}

¹The Hong Kong University of Science and Technology ²Nanjing University

³Southern University of Science and Technology ⁴Shanghai AI Laboratory

⁵Shanghai TechWind Technology Co., Ltd.

*Equal contribution §Corresponding authors †Project lead

Abstract

Accurate evaluation of weather forecasting models is critical for their reliable deployment in real-world applications. However, existing benchmarks predominantly rely on reanalysis products such as ERA5, which are generated through delayed data assimilation and do not reflect the constraints of real-time operational forecasting, thereby resulting in a systematic mismatch between benchmark performance and real-world forecasting. In this work, we introduce RealBench, a next-generation benchmark for AI weather forecasting that emphasizes realistic evaluation under operational conditions. RealBench features a strictly out-of-distribution test set spanning 2025 to eliminate data leakage and capture recent atmospheric regimes. It integrates multiple data sources, including low-latency operational analysis and a large-scale global in-situ observation dataset comprising over 10,000 stations, enabling direct evaluation against real atmospheric measurements. Beyond standard global metrics, RealBench provides a comprehensive evaluation framework for high-impact extreme events, including heatwaves, cold surges, and tropical cyclones, using event-specific metrics that better reflect real-world forecasting priorities. The evaluation results reveal substantial discrepancies between reanalysis-based metrics and real-world performance, particularly concerning extreme events. By highlighting the limitations of existing benchmarks, this work establishes a more faithful and operationally relevant evaluation paradigm, providing a rigorous foundation for advancing next-generation AI weather forecasting systems. The benchmark implementation is available at: <https://github.com/lixrui-del/NWP-Benchmark>.

Corresponding: songguo@ust.hk; bailei@pjlab.org.cn

Key finding!!! RealBench reveals that strong ERA5 scores do not guarantee operational readiness; station observations and extreme-event metrics expose the largest real-world performance gaps.

arXiv:2605.24945v1 [cs.LG] 24 May 2026

Contents

1	Introduction	3
2	Related Work	3
3	Dataset	4
4	RealBench: Benchmark Design and Evaluation Settings	5
5	Experimental Results	7
5.1	Comparison of Medium-range Weather Forecasts	7
5.2	Extreme Events Assessment	7
6	Discussion	9
7	Conclusion	11
A	Limitations	15
B	Broader Impacts	15
C	Details of WEATHER-10K	15
C.1	Station Distribution and Country-level Statistics	15
C.2	Data Preprocessing	16
C.3	Quality Control with ERA5 Reference Fields.....	16
D	Additional Experimental Details	16
D.1	Baseline Models	16
D.2	Complete List of Variables	17
D.3	Evaluation Metrics	17
D.4	Implementation Details	18
D.5	More Experimental Results	19

1 Introduction

Accurate weather forecasting is a critical challenge with profound socioeconomic implications, directly impacting sectors such as aviation, maritime navigation, and finance [1–3]. Recent advances in deep learning have enabled AI-based weather forecasting methods [4–7] to achieve performance comparable to traditional numerical weather prediction (NWP) systems, while offering substantially faster inference. Despite this rapid progress, a critical question remains underexplored: **Do current evaluation protocols faithfully reflect the performance of AI-based models under real-world operational conditions with observational data?**

Currently, the answer is often no. While existing evaluation paradigms [8–13] have significantly advanced standardized assessments for AI weather forecasting, they remain limited in their ability to reflect real-world, operational conditions. Several design choices contribute to this discrepancy. 1) Their reliance on relatively early test periods (*e.g.*, 2020) raises concerns regarding potential data leakage and temporal representativeness, as models are not evaluated on the latest atmospheric regimes or emerging distribution shifts. 2) They predominantly adopt ERA5 reanalysis data [14] as the ground truth rather than real-time operational conditions or real-world station observations. As a model-informed, temporally lagged 4D-Var data assimilation product, ERA5 inherently introduces biases and may underestimate localized extremes, such as temperature peaks and tropical cyclone intensity. 3) Their heavy reliance on global average metrics (*e.g.*, RMSE) emphasizes common large-scale patterns while obscuring performance on rare but high-impact extreme events. Although recent works [15, 16] have begun incorporating real station observations to better approximate real-world conditions, they rely on a limited number of stations with sparse spatial coverage and evaluate only a small set of models, falling short of a comprehensive and systematic quantification of these biases.

To systematically bridge the gap between benchmark scores and real-world utility, we introduce **RealBench**, a next-generation benchmark for evaluating AI weather models under realistic operational conditions, which reconstructs the evaluation pipeline by shifting from historical, reanalysis-dependent metrics to operational, observation-grounded assessments. RealBench provides a comprehensive evaluation protocol that isolates models from training data leakage, replaces temporally lagged reference fields with real-time operational analysis and dense global station observations, and introduces targeted protocols specifically formulated to capture high-impact extreme weather events.

We make four core contributions: **(i) Recent zero-leakage evaluation (2025)**. We construct a strictly out-of-distribution test set covering 2025, ensuring no exposure to existing training data. This provides a more up-to-date evaluation that reflects current atmospheric regimes and recent distribution shifts. **(ii) Evaluation on operational analysis data**. We introduce an ECMWF operational analysis dataset that reflects near real-time forecasting conditions with substantially lower latency than ERA5. Systematically evaluating state-of-the-art data-driven models on this dataset reveals notable discrepancies compared to ERA5-based evaluations, highlighting the necessity of operational data. **(iii) Evaluation on WEATHER-10K station observations**. We evaluate models using WEATHER-10K, a large-scale global dataset comprising over 10,000 in-situ stations sourced from the Global Historical Climatology Network hourly (GHCNh), complete with rigorous preprocessing (*e.g.*, outlier correction). This enables a more direct assessment against real atmospheric observations with significantly improved spatial coverage. **(iv) Comprehensive evaluation of extreme events and an open-source framework**. We systematically evaluate extreme, high-impact weather events, including heatwaves, cold surges, and tropical cyclones. For temperature extremes, we adopt a sliding-window approach across a 12-year climatology to define event thresholds (90th/10th percentiles). For tropical cyclones, we evaluate all 2025 events using track, mean sea level pressure (MSL), and wind speed errors. Furthermore, we open-source a user-friendly unified PyTorch inference framework to support seamless evaluation across multiple state-of-the-art AI forecasting models.

Ultimately, RealBench establishes a rigorous and realistic evaluation framework for next-generation AI weather forecasting systems. By explicitly grounding evaluations in real-time constraints, real-world observations, and the precise assessment of high-impact extreme events, RealBench successfully bridges the critical gap between theoretical benchmark performance and practical forecasting utility.

2 Related Work

Benchmark Datasets for Weather and Climate Modeling. Recent works have developed benchmarks for climate modeling across a range of tasks. WeatherBench [9] introduced a standardized ERA5-based benchmark for medium-range forecasting and was later extended to probabilistic settings [17]; WeatherBench2 [10] further improves resolution, metrics, scalability, and baseline comparisons. Other benchmarks address subseasonal forecasting [18], precipitation forecasting [19, 20], extreme-event analysis [21–25], and unified multi-task evaluation [26]. Recent datasets such as

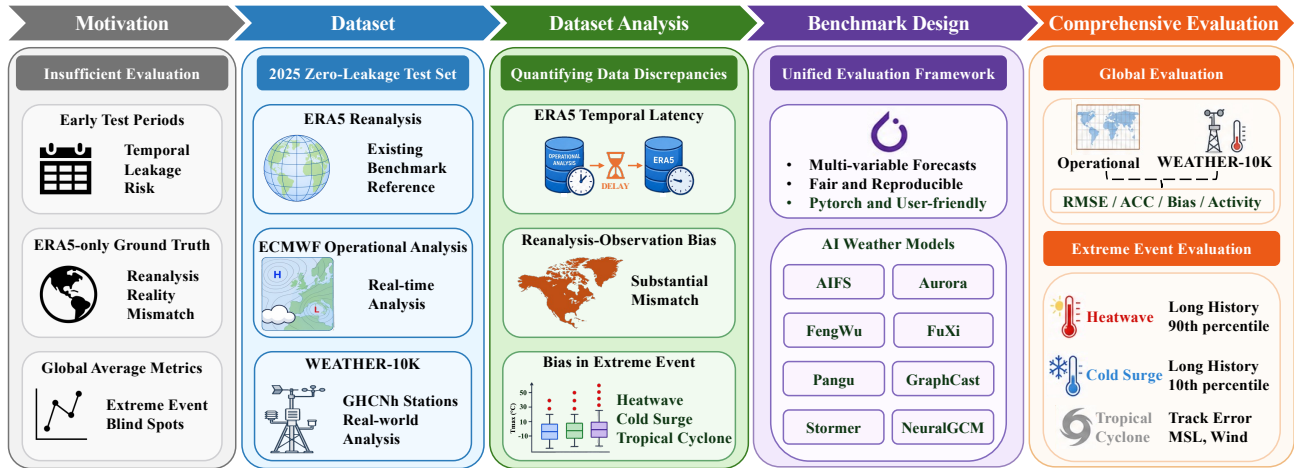


Figure 1. Overview of RealBench, illustrating a real-world and real-time benchmarking pipeline for evaluating AI weather models in operational forecasting settings.

WeatherReal [15] incorporate in-situ observations, but remain limited in spatial coverage and evaluation scope. Additional benchmarks focus on modeling components and long-term behavior [27, 28].

Despite this progress, existing benchmarks exhibit two key limitations: they predominantly rely on reanalysis or simulated data (e.g., ERA5 [14], CMIP6 [29]) that fail to capture real-world operational constraints, and their reliance on aggregate metrics often under-characterizes extreme events. To our knowledge, we introduce the first standardized benchmark for AI weather models that systematically unifies medium-range and high-impact forecasting. By evaluating models on real-time, real-world data, our framework enables a more faithful assessment of true operational capabilities.

AI-based Weather Forecasting. With the rapid rise of deep learning [30–37], data-driven weather modeling has rapidly elevated forecasting capabilities across a diverse range of meteorological tasks. Early milestones primarily concentrated on deterministic global medium-range forecasting [4, 6, 38, 39, 7, 8, 11, 40, 41], quickly achieving parity with or surpassing traditional numerical weather prediction (NWP) systems. Building upon these foundations, subsequent research has broadened the operational scope of AI models. This includes the development of generative and ensemble approaches for uncertainty quantification [5, 42–51], as well as the integration of data assimilation directly into end-to-end learning pipelines [52, 53]. Furthermore, the field has expanded to tackle extended forecasting horizons and specialized scenarios, such as high-resolution downscaling [54], extreme weather prediction [55], and long-term climate simulation [56]. Most recently, the paradigm has shifted toward large-scale foundation and hybrid models [57–60], which synthesize massive multi-source datasets to provide versatile, general-purpose meteorological forecasting engines.

3 Dataset

ERA5 and Operational Analysis Data. As shown in Figure 1, we evaluate models on both ERA5 reanalysis [14] and ECMWF operational analysis data. ERA5 provides hourly global reanalysis at 0.25° resolution from 1940 to near-present, generated by a 4D-Var assimilation system with 12-hour windows. This extended window improves retrospective consistency but introduces substantial latency and information unavailable under strict real-time forecasting. In contrast, ECMWF operational analyses use a shorter ± 3 -hour 4D-Var window around initialization, relying on near-real-time observations for low-latency production. Thus, ERA5 serves as a high-quality retrospective reference, whereas operational analysis data better reflect information availability in real-time settings.

WEATHER-10K. WEATHER-10K is derived from global near-surface in-situ observations provided by the Global Historical Climatology Network hourly dataset (GHCN_h). GHCN_h is a next-generation hourly dataset consisting of surface weather measurements from fixed, land-based stations, compiled from multiple sources maintained by NOAA, the U.S. Air Force, and other meteorological agencies, and harmonized into a unified format. The resulting dataset contains observations from over 10,000 stations, providing extensive spatial coverage across diverse geographic regions, albeit with substantial geographic imbalance in station density. Further details on station distribution, country-level statistics, and data preprocessing procedures are provided in Appendix C.

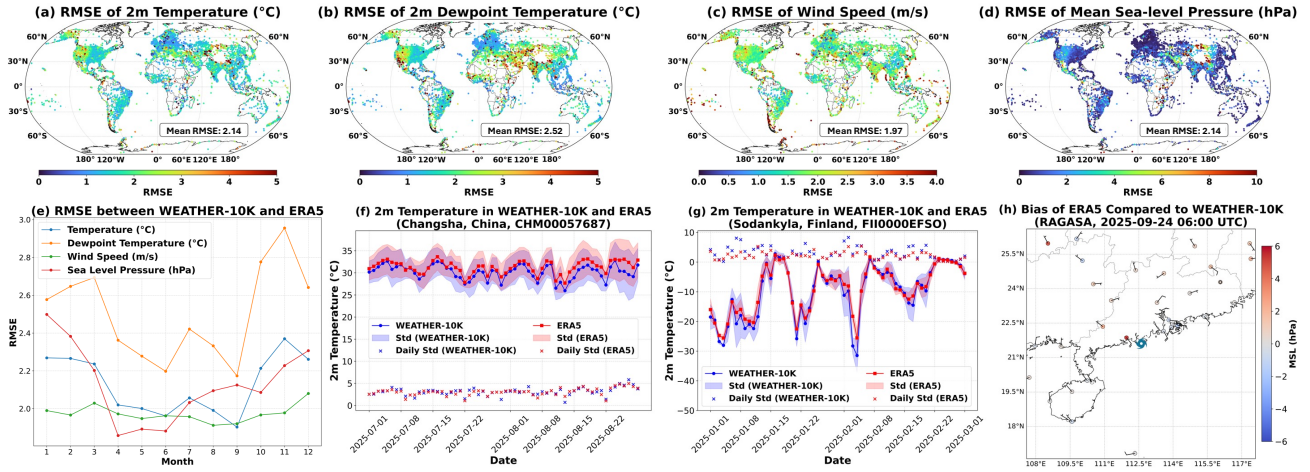


Figure 2. Data analysis and visualizations. (a–d) Global RMSE in 2025 for T2M, D2M, wind speed, and MSL. (e) Monthly RMSE of the four variables in 2025. (f–g) T2M comparisons during heatwave and cold surge periods at Changsha, China, and Sodankylä, Finland. (h) Bias of ERA5 relative to WEATHER-10K in MSL, wind speed, and wind direction for Typhoon Ragasa.

Dataset Analysis. As shown in Figure 2(a)–(e), we compute the RMSE between WEATHER-10K and ERA5 in 2025 across four near-surface variables. Overall, T2M and D2M exhibit moderate errors with mean RMSEs of 2.14°C and 2.52°C, respectively, and show larger discrepancies over regions with complex terrain or heterogeneous surface conditions. Wind speed shows comparable mean error magnitude (1.97 m/s) but stronger spatial variability, reflecting the difficulty of resolving near-surface winds affected by local topography, surface roughness, and boundary-layer processes. In contrast, MSL has the lowest overall discrepancy, with a mean RMSE of 2.14 hPa and broadly smoother spatial patterns, consistent with the stronger large-scale constraints on pressure fields. The monthly RMSE curves further indicate that the discrepancies are seasonally dependent, with D2M showing the largest temporal variation among the four variables.

Figure 2(f)–(h) further examines WEATHER-10K and ERA5 under representative extreme-weather conditions. During the summer heatwave period in Changsha, China, and the winter cold surge period in Sodankylä, Finland, the two datasets generally capture similar T2M temporal evolution, while local deviations remain evident at daily time scales. These deviations highlight the challenge of matching station-level temperature extremes, especially when sub-grid surface effects and local meteorological variability become important. For Typhoon Ragasa, the spatial bias map of MSL, wind speed, and wind direction shows structured differences between ERA5 and WEATHER-10K around the storm-affected region, suggesting that discrepancies during tropical cyclones are not purely random but are linked to the representation of storm-scale pressure and wind structures.

Overall, these results reveal variable- and region-dependent gaps between ERA5 and in-situ observations. While ERA5 provides spatially complete and dynamically consistent fields, it can smooth local variability captured by WEATHER-10K, highlighting the need for station-based evaluation.

4 RealBench: Benchmark Design and Evaluation Settings

Problem Formulation. We formulate global medium-range weather forecasting as a spatiotemporal prediction problem over gridded atmospheric states. Let $X_t \in \mathbb{R}^{C \times H \times W}$ denote the atmospheric state at time t , where C is the number of atmospheric variables and $H \times W$ is the spatial resolution. Given the current state X_t , the objective is to learn a parametric model F_θ that predicts future states over a horizon T , *i.e.*, $\hat{X}_{t+1:t+T} = F_\theta(X_t)$. Forecasting is often performed in an autoregressive manner, where $\hat{X}_{t+k} = F_\theta(\hat{X}_{t+k-1})$ for $k = 1, \dots, T$. The model is trained to minimize the discrepancy between predictions \hat{X}_{t+k} and ground-truth states X_{t+k} over the forecast horizon.

Baselines. We compare representative state-of-the-art AI-based global weather forecasting models, including AIFS [59], Aurora [57], GraphCast [4], Pangu-Weather [8], FuXi [13], FengWu [61], Stormer [12], and NeuralGCM [56]. For all baseline models, inference is conducted using their officially released, open-source checkpoints; the specific model checkpoint versions utilized for both ERA5-based and IFS-based inference in this benchmark are detailed in Table 4. Detailed descriptions of each baseline model architecture are provided in Appendix D.1.

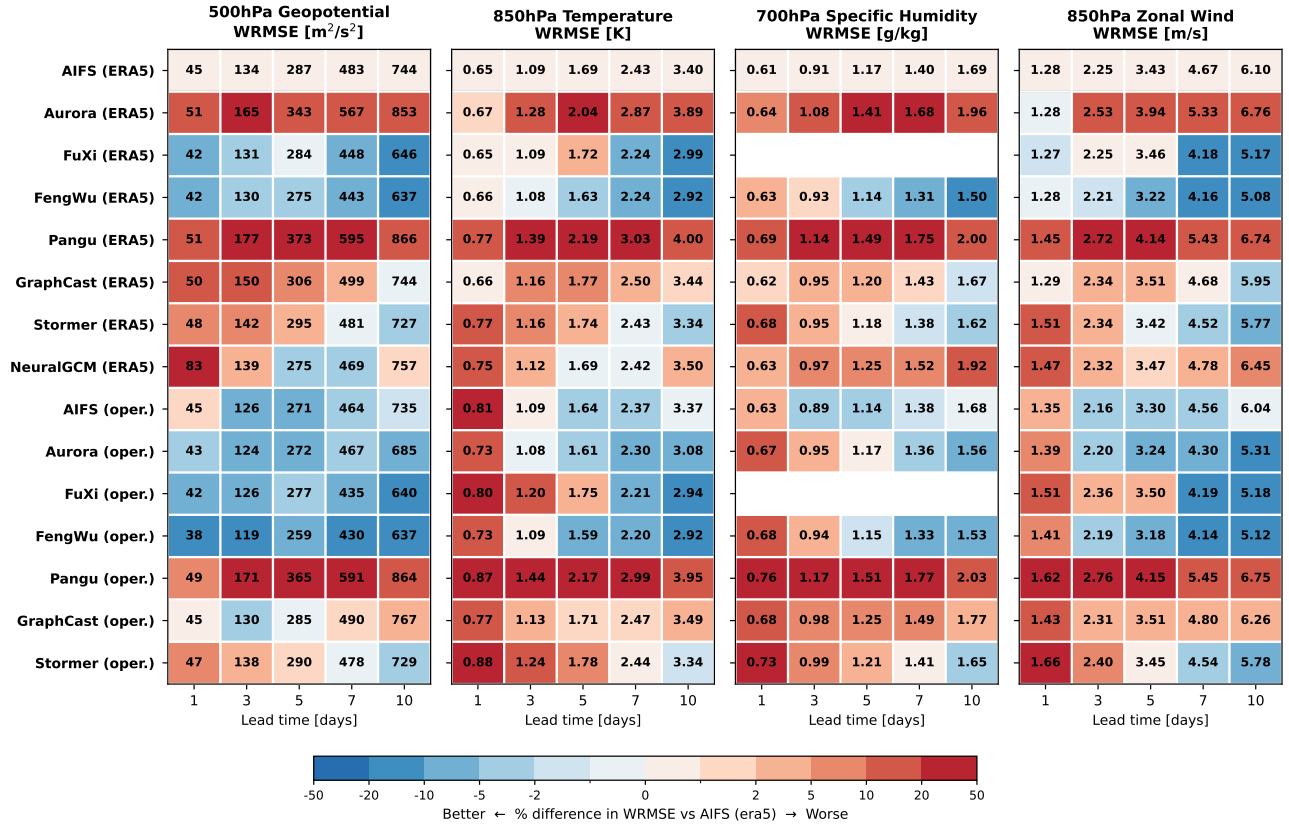


Figure 3. Scorecard for upper-level variables for the year 2025. (oper.) Operational models are evaluated against operational analysis.

Evaluation Setup and Metrics. We evaluate model performance on the year 2025 using three datasets: ERA5, operational analysis data, and WEATHER-10K with a 6-hour temporal resolution. For tropical cyclones, we comprehensively evaluate all 72 events occurring from June to December 2025. Forecasts are generated up to a 10-day lead time (*i.e.*, 40 autoregressive steps at 6-hour intervals). To ensure consistent evaluation across models with varying native resolutions, all model outputs are interpolated to a uniform 0.25° grid. Following standard practice, we assess performance on eight key atmospheric variables: 2-meter temperature (T2M), 10-meter zonal and meridional winds (U10, V10), mean sea level pressure (MSL), geopotential height at 500 hPa (Z500), temperature at 850 hPa (T850), specific humidity at 700 hPa (Q700), and 850 hPa zonal wind speed (U850). Forecast accuracy is evaluated using four latitude-weighted spatial metrics: weighted root-mean-square error (WRMSE) [54], bias, anomaly correlation coefficient (ACC), and activity. Furthermore, we compute the zonal energy spectrum to assess the physical realism of the forecasts across different spatial scales. The full variable list and metric definitions are provided in Appendix D.2 and Appendix D.3. Further implementation details and computational cost comparisons are provided in Appendix D.4 and Table 5.

Heatwaves and Cold Surges Evaluation. Following prior work on temperature extremes [62], we evaluate predicted heatwave and cold surge events using a percentile-based event definition and an IoU-based temporal matching strategy. Detailed definitions of the extreme-event thresholds, consecutive-day criteria, and event matching procedure are provided in Appendix D.3. Based on the matched predicted and ground-truth events, we employ three standard metrics [63]: Probability of Detection (POD), False Alarm Ratio (FAR), and Critical Success Index (CSI), defined as

$$\text{POD} = \frac{\text{TP}}{\text{TP} + \text{FN}}, \quad \text{FAR} = \frac{\text{FP}}{\text{TP} + \text{FP}}, \quad \text{CSI} = \frac{\text{TP}}{\text{TP} + \text{FP} + \text{FN}}. \quad (1)$$

POD measures the fraction of observed events that were correctly forecast, FAR quantifies the fraction of predicted events that did not occur, and CSI provides a balanced assessment by penalizing both misses and false alarms while ignoring the overwhelmingly large number of true negatives characteristic of rare extreme events.

Tropical Cyclones. To ensure a fair comparison, the metrics at a specific lead time l are averaged only over the subset of storms, denoted as S_l , that are successfully tracked by all evaluated models. Given the predicted and observed cyclone

centers $(\hat{\phi}_{s,l}, \hat{\lambda}_{s,l})$ and $(\phi_{s,l}, \lambda_{s,l})$ for storm s at lead time l , the direct position error (DPE) is measured by the average great-circle distance:

$$\text{DPE}_l = \frac{1}{|\mathcal{S}_l|} \sum_{s \in \mathcal{S}_l} d_{\text{gc}}((\hat{\phi}_{s,l}, \hat{\lambda}_{s,l}), (\phi_{s,l}, \lambda_{s,l})), \quad (2)$$

where $d_{\text{gc}}(\cdot, \cdot)$ denotes the haversine distance on the sphere.

We additionally evaluate intensity errors using the maximum 10-meter wind speed (V) and minimum sea-level pressure (P^{min}). Since data-driven models often suffer from structural under-intensification (*i.e.*, producing smoother fields), we report both the Mean Absolute Error (MAE) and the systematic Bias at each lead time l :

$$\text{MAE}_l^P = \frac{1}{|\mathcal{S}_l|} \sum_{s \in \mathcal{S}_l} |\hat{P}_{s,l}^{\text{min}} - P_{s,l}^{\text{min}}|, \quad \text{Bias}_l^P = \frac{1}{|\mathcal{S}_l|} \sum_{s \in \mathcal{S}_l} (\hat{P}_{s,l}^{\text{min}} - P_{s,l}^{\text{min}}). \quad (3)$$

The wind speed errors (MAE_l^V and Bias_l^V) are formulated analogously.

5 Experimental Results

5.1 Comparison of Medium-range Weather Forecasts

Upper-level Evaluation. As shown in Figure 3, FengWu and FuXi achieve the strongest overall performance across most upper-level variables and lead times, especially at medium-to-long ranges. For Z500, FengWu (oper.) obtains the lowest RMSE from 1 to 10 days, with values of 38, 119, 259, 430, and 637 m^2/s^2 , while FuXi (oper.) remains highly competitive, reaching 435 and 640 m^2/s^2 at 7 and 10 days, respectively. For T850, FengWu (oper.) also achieves the best or near-best results, with RMSEs of 2.20 K and 2.92 K at 7 and 10 days. Similar trends are observed for Q700 and U850, where FengWu maintains strong long-range accuracy. Overall, the upper-level results indicate that operational-analysis evaluation preserves the relative ranking of leading models, with FengWu and FuXi consistently providing the most accurate forecasts among the compared systems.

Surface Evaluation. As shown in Figure 4, the results include ERA5, operational-analysis, and WEATHER-10K station-based evaluations, where ‘oper.’ denotes operational analysis data. On ERA5 and operational-analysis data, FengWu and FuXi remain the strongest models across most variables, especially at longer lead times. For example, FengWu (ERA5) achieves 2.28 K for 2-meter temperature (T2M), 3.49 m/s for 10-meter zonal wind (U10), 3.67 m/s for 10-meter meridional wind (V10), and 587.88 Pa for mean sea-level pressure (MSL) at 10 days. Under the operational setting, FengWu obtains 2.40 K, 3.59 m/s, 3.78 m/s, and 591.41 Pa at 10 days for the same variables, while FuXi is particularly competitive for T2M and MSL. On WEATHER-10K station evaluation, the RMSE is larger, reflecting the increased difficulty of pointwise station verification. This discrepancy is expected, since a natural mismatch already exists between analysis data and station observations (as shown in Figure 2). Consequently, AI models trained with ERA5 as the ground truth inevitably inherit such discrepancies when evaluated against real station measurements. This observation further indicates that forecasting on irregularly distributed stations is inherently challenging, and highlights the necessity of station-based evaluation under real-world conditions.

Cross-Dataset ACC Comparison. As shown in Figure 5, we compare AI-based models using ACC across ERA5, operational analysis data, and WEATHER-10K. ACC decreases with increasing lead time, and performance gaps become more pronounced at longer horizons. Compared with gridded ERA5 and IFS evaluations, station-based surface evaluation yields lower ACC, especially for near-surface winds, indicating the challenge of forecasting on irregularly distributed stations and the necessity of real-world station-based evaluation. More results are presented in the Appendix D.5.

5.2 Extreme Events Assessment

Heatwaves. Table 1 details the performance on global heatwave events during the second half of 2025. Overall, forecasting skill declines as lead time increases, with AIFS consistently performing best. Specifically, we observe the following key phenomena: **(i) Precision-Recall Trade-offs.** The detailed metrics reveal varying characteristics among the architectures. Most models exhibit a conservative tendency, maintaining relatively high precision (low False Alarm Ratio, FAR) but suffering from lower recall (Probability of Detection, POD) at early lead times. FengWu exemplifies this robustness, maintaining the lowest FAR globally at extended lead times (*e.g.*, 0.447 at Day 7). This suggests that models hesitate to predict extreme heat objects unless the large-scale circulation signal is overwhelmingly strong. **(ii) Detail Loss at Long**

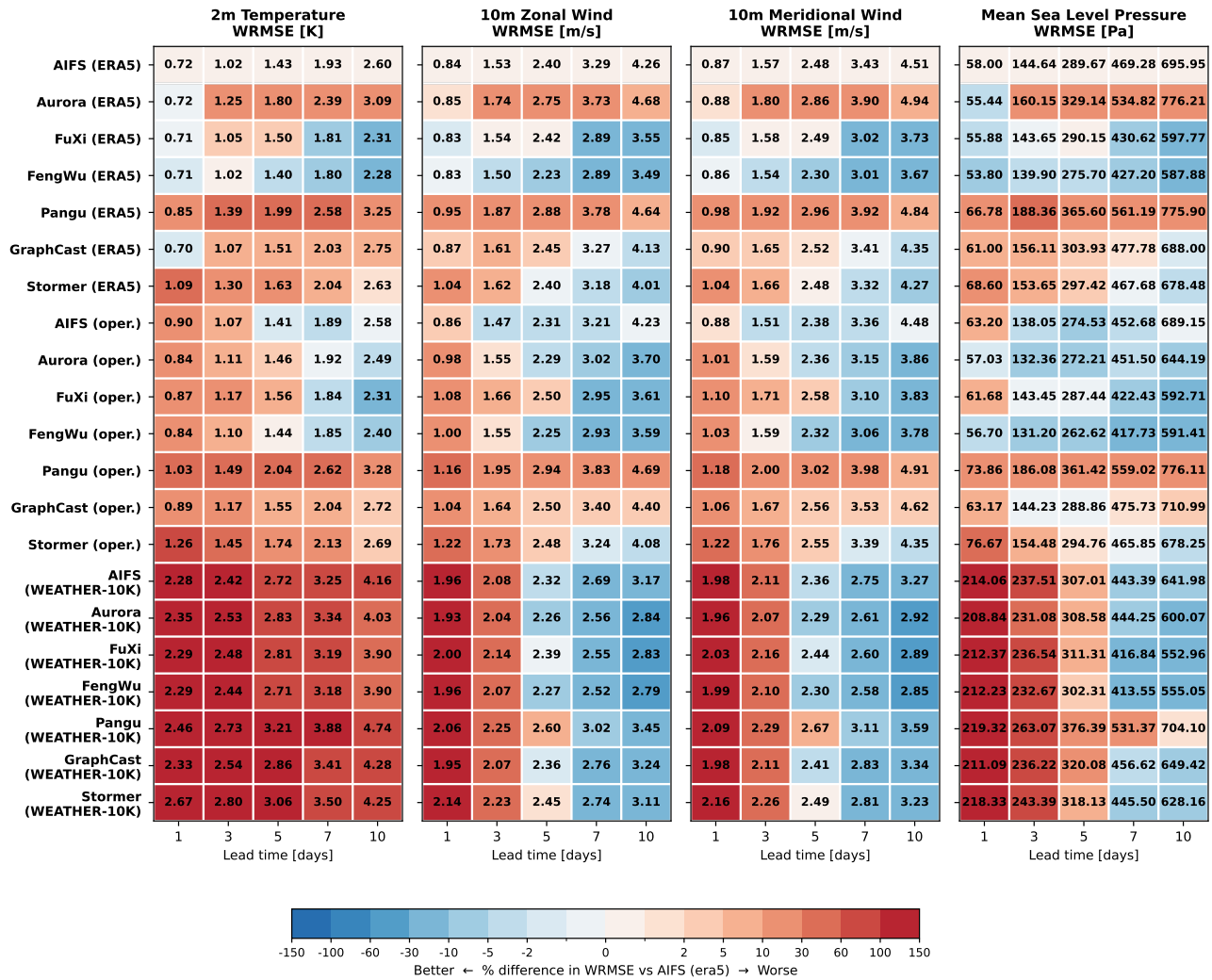


Figure 4. Scorecard for surface-level variables for the year 2025. (oper.) Operational models are evaluated against operational analysis. (WEATHER-10K) WRMSE computed between station observations and operational forecast outputs interpolated to station locations.

Lead Times. Beyond Day 7, forecasting skill for extreme heat declines significantly. By Day 10, most models drop below a CSI of 0.17 (e.g., Pangu-Weather drops to 0.086). This performance degradation may be attributed to the tendency of RMSE optimization to smooth spatial gradients, which underestimates heatwave intensity at extended lead times. This smoothing effect is empirically demonstrated by the systematic negative biases in the case studies (see Appendix Figure 21).

Cold Surges. A direct comparison in Table 1 reveals that the performance degradation observed in heatwaves is also present in cold surges, but the overall performance is worse. For instance, the Day 1 CSI for the best-performing model (AIFS) drops from 0.513 (heatwaves) to 0.370 (cold surges). At extended lead times (Day 7 and Day 10), the FAR for cold surges increases rapidly across multiple models. Interestingly, while Pangu-Weather achieves the highest POD at Day 3 (0.599) and Day 7 (0.414) for cold surges, it simultaneously produces a FAR of 0.633 and 0.909, respectively. It captures cold events through over-prediction, resulting in a large number of false positives among its predicted cold objects.

This asymmetric performance may stem from an imbalanced target distribution in the training data. Under the recent global warming trend, extreme cold anomalies relative to the 1979–1990 climatological baseline are significantly rarer in the recent training data than extreme heatwaves. Consequently, models are generally less capable of forecasting cold surges. When predicting these events, models tend to overly smooth the outputs. This can either cause forecasts to miss the strict P10 threshold (leading to low POD), or generate temporally and spatially smoothed events that fail to overlap with the ground truth under the temporal IoU metric (leading to high FAR). As shown in Appendix Figure 22, this smoothing causes an overall positive bias during cold surges (i.e., predicting temperatures too warm for cold extremes).

Model	Metric	Heatwave (2025 H2)				Cold Surge (2025 H2)			
		Day 1	Day 3	Day 7	Day 10	Day 1	Day 3	Day 7	Day 10
AIFS	CSI \uparrow	0.513	0.535	0.353	0.215	0.370	0.413	0.234	0.131
	POD \uparrow	0.646	0.689	0.533	0.399	0.443	0.526	0.348	0.249
	FAR \downarrow	0.291	0.311	0.489	0.673	0.294	0.347	0.585	0.774
FengWu	CSI \uparrow	0.486	0.486	0.279	0.136	0.358	0.390	0.196	0.060
	POD \uparrow	0.615	0.628	0.368	0.189	0.432	0.522	0.260	0.075
	FAR \downarrow	0.301	0.327	0.447	0.620	0.312	0.394	0.548	0.723
FuXi	CSI \uparrow	0.470	0.423	0.283	0.168	0.344	0.372	0.201	0.064
	POD \uparrow	0.632	0.685	0.472	0.281	0.433	0.544	0.295	0.092
	FAR \downarrow	0.355	0.483	0.573	0.672	0.356	0.459	0.609	0.795
Pangu	CSI \uparrow	0.458	0.381	0.165	0.086	0.342	0.290	0.075	0.028
	POD \uparrow	0.628	0.598	0.296	0.172	0.410	0.599	0.414	0.244
	FAR \downarrow	0.373	0.479	0.667	0.782	0.313	0.633	0.909	0.965
Aurora	CSI \uparrow	0.450	0.443	0.252	0.132	0.331	0.348	0.132	0.024
	POD \uparrow	0.586	0.606	0.347	0.199	0.417	0.513	0.204	0.039
	FAR \downarrow	0.332	0.379	0.483	0.668	0.368	0.474	0.715	0.922
GraphCast	CSI \uparrow	0.437	0.392	0.259	0.160	0.316	0.328	0.200	0.085
	POD \uparrow	0.588	0.595	0.452	0.326	0.397	0.488	0.350	0.204
	FAR \downarrow	0.364	0.448	0.592	0.732	0.383	0.501	0.681	0.865
Stormer	CSI \uparrow	0.426	0.432	0.275	0.169	0.305	0.332	0.183	0.087
	POD \uparrow	0.536	0.574	0.403	0.277	0.388	0.456	0.291	0.174
	FAR \downarrow	0.313	0.364	0.510	0.661	0.381	0.437	0.655	0.838

Table 1. Detailed verification metrics (CSI, POD, FAR) across 1 to 10 lead days with multiple models.

Tropical Cyclones. Table 2 presents the homogeneous sample evaluation of tropical cyclone track and intensity forecasts during the second half of 2025. In terms of track prediction (Track DPE), all models demonstrate high accuracy at early lead times (Day 1), with errors ranging between 50 and 70 km. As the forecast lead time extends to Day 5, model performance diverges; notably, GraphCast and Stormer maintain relatively low track errors of approximately 300–320 km. Furthermore, comparing the results initialized with ERA5 and IFS reveals that models fine-tuned on operational IFS data (e.g., Aurora and AIFS) exhibit significant reductions in track errors when evaluated with IFS initializations. For instance, Aurora’s Day-5 track error drops from 427.6 km (ERA5) to 338.1 km (IFS). Conversely, models without specific operational adaptation (e.g., Pangu-Weather) perform similarly across both initialization datasets. This directly demonstrates the necessity of conducting benchmark evaluations under realistic operational conditions.

Compared to track prediction, current data-driven models generally exhibit notable shortcomings in forecasting cyclone intensity. Across all lead times, the evaluated models produce substantial positive biases in minimum sea level pressure (MSLP biases ranging from +10.1 to +39.5 hPa), along with considerable wind speed errors. This indicates a systematic underestimation of the true cyclone intensity. Notably, the magnitude of this intensity degradation varies among models, largely constrained by their different resolutions. For example, Stormer, which operates at a coarser native resolution of 1.4°, exhibits the largest MSLP bias. These results suggest that while current AI models can accurately capture tropical cyclone trajectories, precisely representing and maintaining their extreme intensity remains a core challenge for future development.

6 Discussion

The primary objective of this work is to evaluate the forecasting performance of data-driven global weather models under operational constraints and against in-situ station observations [10, 15]. Reanalysis datasets such as ERA5, although widely used for benchmarking, are generated through delayed data assimilation and do not fully reflect the constraints of real-time operational forecasting [14]. To address this discrepancy, we present *RealBench*, an evaluation framework that integrates near-real-time ECMWF operational analysis and a global ground-based observation dataset (*WEATHER-10K*). The evaluation reveals substantial discrepancies between reanalysis-based metrics and operational performance, particularly during extreme events, thereby bridging the gap between theoretical benchmark performance and practical forecasting utility [10, 15].

Our results indicate a systematic performance degradation when transitioning from ERA5-based verification to operational analyses. Reanalysis products utilize a temporally lagged, retrospective data assimilation process (such as a 12-hour 4D-Var window) that optimizes global dynamical consistency by incorporating retrospective observations [14]. Data-driven models

Model	Metric	ERA5 Initialized			IFS Initialized		
		Day 1	Day 3	Day 5	Day 1	Day 3	Day 5
AIFS	Track DPE (km) ↓	54.7	154.1	428.3	52.7	138.2	366.3
	MSLP MAE (hPa) ↓	11.5	16.8	18.2	10.7	16.1	16.2
	MSLP Bias (hPa)	+11.1	+16.2	+16.8	+10.1	+15.4	+14.3
	Wind MAE (m/s) ↓	14.3	17.8	17.6	13.6	17.4	15.9
Aurora	Track DPE (km) ↓	55.7	148.7	427.6	51.6	133.9	338.1
	MSLP MAE (hPa) ↓	12.3	17.3	17.8	11.4	20.1	29.1
	MSLP Bias (hPa)	+11.9	+15.2	+15.1	+10.8	+20.0	+29.1
	Wind MAE (m/s) ↓	13.9	16.4	15.2	13.5	19.5	22.5
FengWu	Track DPE (km) ↓	58.3	163.9	409.4	56.2	140.6	371.0
	MSLP MAE (hPa) ↓	14.4	24.2	39.5	13.1	21.9	29.9
	MSLP Bias (hPa)	+14.3	+24.1	+39.5	+12.8	+21.5	+29.8
	Wind MAE (m/s) ↓	15.9	22.6	29.5	14.9	21.0	24.7
FuXi	Track DPE (km) ↓	57.3	152.4	360.2	78.1	181.7	331.0
	MSLP MAE (hPa) ↓	13.8	20.0	22.8	13.8	19.7	18.2
	MSLP Bias (hPa)	+13.6	+19.5	+22.6	+13.5	+19.2	+17.9
	Wind MAE (m/s) ↓	15.3	19.2	19.0	14.6	18.8	16.8
GraphCast	Track DPE (km) ↓	59.1	149.1	320.3	52.9	135.4	371.0
	MSLP MAE (hPa) ↓	13.7	21.1	26.1	11.1	18.4	17.8
	MSLP Bias (hPa)	+13.5	+20.7	+26.1	+10.3	+17.3	+16.2
	Wind MAE (m/s) ↓	15.9	21.0	22.2	13.9	18.5	16.9
Pangu	Track DPE (km) ↓	64.5	185.9	444.7	66.0	189.2	428.8
	MSLP MAE (hPa) ↓	14.5	21.3	25.9	14.3	20.3	20.3
	MSLP Bias (hPa)	+14.3	+20.7	+25.7	+14.1	+19.8	+19.9
	Wind MAE (m/s) ↓	15.2	19.2	20.1	14.9	18.7	17.1
Stormer	Track DPE (km) ↓	69.5	155.2	320.0	68.9	151.3	304.9
	MSLP MAE (hPa) ↓	15.8	23.3	29.0	15.4	21.9	22.8
	MSLP Bias (hPa)	+15.7	+23.2	+29.0	+15.3	+21.8	+22.7
	Wind MAE (m/s) ↓	17.7	22.2	23.4	17.2	21.6	20.8

Table 2. Typhoon track and intensity verification over a homogeneous sample set for ERA5- and IFS-initialized forecasts at 1-, 3-, and 5-day lead times.

optimized primarily on these highly consistent, smoothed reanalysis fields exhibit a degree of overfitting to these idealized gridded structures. Consequently, when evaluated against near-real-time ECMWF operational analysis, which operates under strict latency constraints and a shorter assimilation window, or against high-frequency physical ground observations, these models exhibit a drop in accuracy. This indicates that theoretical excellence on retrospectively consistent reanalysis fields does not consistently translate to real-world forecasting utility under operational constraints.

These performance discrepancies are further pronounced during high-impact extreme weather events. In our evaluation of global heatwaves, several models show increasingly negative T_{\max} biases at longer lead times during the strongest events, indicating a reduction in peak intensity fidelity as lead time increases (as shown in Figure 21). Conversely, for global cold surges, the model spread increases with lead time, and a positive T_{\min} bias becomes more common at longer leads, corresponding to weaker simulated cold intensity relative to ERA5 (as shown in Figure 22). This systematic underestimation of extreme peaks is consistent with the spatial smoothing effect induced by optimizing global spatial fields using mean-squared error (MSE) or weighted grid-cell loss functions. Such mathematical optimizations naturally suppress localized peak gradients and high-frequency temporal variances, leading to a general underestimation of extreme value magnitudes.

Several distinct limitations of the *RealBench* framework must be outlined. First, the geographic density of the *WEATHER-10K* ground station network is highly imbalanced (as shown in Figure 6), with dense coverage in North America and Europe but sparse distribution over oceans and high-latitude regions, which constrains the global representativeness of the pointwise metrics. Second, there is a fundamental spatial scale mismatch between the 0.25° gridded model outputs and pointwise physical measurements, which are strongly influenced by sub-grid-scale local topography and surface roughness. Third, to maintain computational efficiency, the temperature extreme thresholds were computed using a 12-year moving climatological window rather than a standard 30-year meteorological baseline, potentially introducing localized regional biases [62].

To address these limitations, future data-driven weather forecasting frameworks should explore hybrid grid-and-point evaluation metrics and local downscaling post-processing. Specifically, integrating statistical lapse-rate temperature adjustments can partially reconcile the scale discrepancy between grid cells and local stations. Furthermore, model training

could incorporate hybrid loss functions that evaluate both grid-scale atmospheric dynamics and point-scale station variations. Future expansions of *RealBench* should focus on incorporating regional high-resolution datasets and probabilistic ensemble systems for operational uncertainty quantification.

7 Conclusion

In this work, we introduced RealBench, a unified benchmark that evaluates data-driven medium-range weather forecasting under zero-leakage 2025 testing, operational analysis, station observations, and extreme-event scenarios. First, RealBench replaces ERA5-only evaluation with ECMWF operational analysis and WEATHER-10K, enabling more realistic verification. Second, RealBench extends evaluation from aggregate forecasting accuracy to high-impact events, including heatwaves, cold surges, and tropical cyclones, using event-specific metrics that reflect practical forecasting priorities. Experiments across representative models reveal substantial discrepancies between reanalysis-based and observation-grounded evaluations, especially for near-surface variables and extremes, highlighting RealBench as a rigorous foundation for advancing operationally reliable forecasts.

References

- [1] Vasudev Dehalwar, Akhtar Kalam, Mohan Lal Kolhe, and Aladin Zayegh. Electricity load forecasting for urban area using weather forecast information. In *2016 IEEE International Conference on Power and Renewable Energy (ICPRE)*, pages 355–359. IEEE, 2016.
- [2] Ismail Gultepe, R Sharman, Paul D Williams, Binbin Zhou, G Ellrod, P Minnis, S Trier, S Griffin, Seong S Yum, B Gharabaghi, et al. A review of high impact weather for aviation meteorology. *Pure and applied geophysics*, 176(5):1869–1921, 2019.
- [3] Kingsley Eghonghon Ukhurebor, Charles Oluwaseun Adetunji, Olaniyan T Olugbemi, W Nwankwo, Akinola Samson Olayinka, C Umezuruike, and Daniel Ingo Hefft. Precision agriculture: Weather forecasting for future farming. In *AI, edge and iot-based smart agriculture*, pages 101–121. Elsevier, 2022.
- [4] Remi Lam, Alvaro Sanchez-Gonzalez, Matthew Willson, Peter Wyrnsberger, Meire Fortunato, Ferran Alet, Suman Ravuri, Timo Ewalds, Zach Eaton-Rosen, Weihua Hu, et al. Learning skillful medium-range global weather forecasting. *Science*, 382(6677):1416–1421, 2023.
- [5] Ilan Price, Alvaro Sanchez-Gonzalez, Ferran Alet, Tom R Andersson, Andrew El-Kadi, Dominic Masters, Timo Ewalds, Jacklynn Stott, Shakir Mohamed, Peter Battaglia, et al. Gencast: Diffusion-based ensemble forecasting for medium-range weather. *arXiv preprint arXiv:2312.15796*, 2023.
- [6] Hao Chen, Han Tao, Guo Song, Jie Zhang, Yunlong Yu, Yonghan Dong, and Lei Bai. Va-moe: Variables-adaptive mixture of experts for incremental weather forecasting. In *Proceedings of the IEEE/CVF International Conference on Computer Vision (ICCV)*, 2025.
- [7] Hao Chen, Tao Han, Jie Zhang, Song Guo, and Lei Bai. Stcast: Adaptive boundary alignment for global and regional weather forecasting. In *Proceedings of the IEEE/CVF Conference on Computer Vision and Pattern Recognition*, 2026.
- [8] Kaifeng Bi, Lingxi Xie, Hengheng Zhang, Xin Chen, Xiaotao Gu, and Qi Tian. Accurate medium-range global weather forecasting with 3d neural networks. *Nature*, 619(7970):533–538, 2023.
- [9] Stephan Rasp, Peter D Dueben, Sebastian Scher, Jonathan A Weyn, Soukayna Moutatadid, and Nils Thuerey. Weatherbench: a benchmark data set for data-driven weather forecasting. *Journal of Advances in Modeling Earth Systems*, 12(11):e2020MS002203, 2020.
- [10] Stephan Rasp, Stephan Hoyer, Alexander Merose, Ian Langmore, Peter Battaglia, Tyler Russell, Alvaro Sanchez-Gonzalez, Vivian Yang, Rob Carver, Shreya Agrawal, et al. Weatherbench 2: A benchmark for the next generation of data-driven global weather models. *Journal of Advances in Modeling Earth Systems*, 16(6):e2023MS004019, 2024.
- [11] Jaideep Pathak, Shashank Subramanian, Peter Harrington, Sanjeev Raja, Ashesh Chattopadhyay, Morteza Mardani, Thorsten Kurth, David Hall, Zongyi Li, Kamyar Azizzadenesheli, et al. Fourcastnet: A global data-driven high-resolution weather model using adaptive fourier neural operators. *arXiv preprint arXiv:2202.11214*, 2022.
- [12] Tung Nguyen, Rohan Shah, Hritik Bansal, Troy Arcomano, Romit Maulik, Veerabhadra Kotamarthi, Ian Foster, Sandeep Madireddy, and Aditya Grover. Scaling transformer neural networks for skillful and reliable medium-range weather forecasting. *Advances in Neural Information Processing Systems*, 37:68740–68771, 2024.
- [13] Lei Chen, Xiaohui Zhong, Feng Zhang, Yuan Cheng, Yinghui Xu, Yuan Qi, and Hao Li. Fuxi: A cascade machine learning forecasting system for 15-day global weather forecast. *npj climate and atmospheric science*, 6(1):190, 2023.
- [14] Hans Hersbach, Bill Bell, Paul Berrisford, Shoji Hirahara, András Horányi, Joaquín Muñoz-Sabater, Julien Nicolas, Carole Peubey, Raluca Radu, Dinand Schepers, et al. The era5 global reanalysis. *Quarterly journal of the royal meteorological society*, 146(730):1999–2049, 2020.

- [15] Weixin Jin, Jonathan Weyn, Pengcheng Zhao, Siqi Xiang, Jiang Bian, Zuliang Fang, Haiyu Dong, Hongyu Sun, Kit Thambiratnam, and Qi Zhang. Weatherreal: a benchmark based on in-situ observations for evaluating weather models. *arXiv preprint arXiv:2409.09371*, 2024.
- [16] Tao Han, Song Guo, Zhenghao Chen, Wanghan Xu, and Lei Bai. Weather-5k: A large-scale global station weather dataset towards comprehensive time-series forecasting benchmark. *arXiv preprint arXiv:2406.14399*, 6(2), 2024.
- [17] Sagar Garg, Stephan Rasp, and Nils Thuerey. Weatherbench probability: A benchmark dataset for probabilistic medium-range weather forecasting along with deep learning baseline models. *arXiv preprint arXiv:2205.00865*, 2022.
- [18] Soukayna Mouatadid, Paulo Orenstein, Genevieve Flaspohler, Miruna Oprescu, Judah Cohen, Franklyn Wang, Sean Knight, Maria Geogdzhayeva, Sam Levang, Ernest Fraenkel, et al. Learned benchmarks for subseasonal forecasting. *arXiv preprint arXiv:2109.10399*, 2021.
- [19] Christian Schroeder de Witt, Catherine Tong, Valentina Zantedeschi, Daniele De Martini, Alfredo Kalaitzis, Matthew Chantry, Duncan Watson-Parris, and Piotr Bilinski. Rainbench: Towards data-driven global precipitation forecasting from satellite imagery. In *Proceedings of the AAAI conference on artificial intelligence*, volume 35, pages 14902–14910, 2021.
- [20] Muhammed Sit, Bong-Chul Seo, and Ibrahim Demir. Iowarain: A statewide rain event dataset based on weather radars and quantitative precipitation estimation. *arXiv preprint arXiv:2107.03432*, 2021.
- [21] Evan Racah, Christopher Beckham, Tegan Maharaj, Samira Ebrahimi Kahou, Mr Prabhat, and Chris Pal. Extremeweather: A large-scale climate dataset for semi-supervised detection, localization, and understanding of extreme weather events. *Advances in neural information processing systems*, 30, 2017.
- [22] Maryam Rahnemoonfar, Tashnim Chowdhury, Argho Sarkar, Debvrat Varshney, Masoud Yari, and Robin Roberson Murphy. Floodnet: A high resolution aerial imagery dataset for post flood scene understanding. *IEEE Access*, 9:89644–89654, 2021.
- [23] Christian Requena-Mesa, Vitus Benson, Markus Reichstein, Jakob Runge, and Joachim Denzler. Earthnet2021: A large-scale dataset and challenge for earth surface forecasting as a guided video prediction task. In *Proceedings of the IEEE/CVF Conference on Computer Vision and Pattern Recognition*, pages 1132–1142, 2021.
- [24] Christoph Minixhofer, Mark Swan, Calum McMeekin, and Pavlos Andreadis. Droughted: A dataset and methodology for drought forecasting spanning multiple climate zones. In *Tackling Climate Change with Machine Learning: Workshop at ICML 2021*, 2021.
- [25] Prabhat, Karthik Kashinath, Mayur Mudigonda, Sol Kim, Lukas Kapp-Schwoerer, Andre Graubner, Ege Karaismailoglu, Leo von Kleist, Thorsten Kurth, Annette Greiner, et al. Climateset: an expert-labelled open dataset and deep learning architecture for enabling high-precision analyses of extreme weather. *Geoscientific Model Development Discussions*, 2020:1–28, 2020.
- [26] Tung Nguyen, Jason Jewik, Hritik Bansal, Prakhar Sharma, and Aditya Grover. Climatelearn: Benchmarking machine learning for weather and climate modeling. *Advances in Neural Information Processing Systems*, 36:75009–75025, 2023.
- [27] Salva Rühling Cachay, Venkatesh Ramesh, Jason NS Cole, Howard Barker, and David Rolnick. Climart: A benchmark dataset for emulating atmospheric radiative transfer in weather and climate models. *arXiv preprint arXiv:2111.14671*, 2021.
- [28] Duncan Watson-Parris, Yuhan Rao, Dirk Olivié, Øyvind Seland, Peer Nowack, Gustau Camps-Valls, Philip Stier, Shahine Bouabid, Maura Dewey, Emilie Fons, et al. Climatebench v1. 0: A benchmark for data-driven climate projections. *Journal of Advances in Modeling Earth Systems*, 14(10):e2021MS002954, 2022.
- [29] Veronika Eyring, Sandrine Bony, Gerald A Meehl, Catherine A Senior, Bjorn Stevens, Ronald J Stouffer, and Karl E Taylor. Overview of the coupled model intercomparison project phase 6 (cmip6) experimental design and organization. *Geoscientific Model Development*, 9(5):1937–1958, 2016.
- [30] Kaiming He, Xiangyu Zhang, Shaoqing Ren, and Jian Sun. Deep residual learning for image recognition. In *Proceedings of the IEEE conference on computer vision and pattern recognition*, pages 770–778, 2016.
- [31] Hao Chen, Yonghan Dong, Zhe-Ming Lu, Yunlong Yu, and Jungong Han. Self-prompting perceptual edge learning for dense prediction. *IEEE Transactions on Circuits and Systems for Video Technology*, 34(6):4528–4541, 2023.
- [32] Lihao Gan, Xin Man, Chenghong Zhang, and Jie Shao. Ewmoe: An effective model for global weather forecasting with mixture-of-experts. In *Proceedings of the AAAI Conference on Artificial Intelligence*, volume 39, pages 210–218, 2025.
- [33] Yuan Gao, Hao Wu, Ruiqi Shu, Huanshuo Dong, Fan Xu, Rui Chen, Yibo Yan, Qingsong Wen, Xuming Hu, Kun Wang, et al. Oneforecast: A universal framework for global and regional weather forecasting. In *Proceedings of the 42th International Conference on Machine Learning*, 2025.
- [34] Hao Chen, Yonghan Dong, Zheming Lu, Yunlong Yu, and Jungong Han. Pixel matching network for cross-domain few-shot segmentation. In *Proceedings of the IEEE/CVF winter conference on applications of computer vision*, pages 978–987, 2024.

- [35] Qi Li, Zhenyu Zhang, Lei Yao, Zhaoxia Li, Tianyi Zhong, and Yong Zhang. Diffusion-based decoupled deterministic and uncertain framework for probabilistic multivariate time series forecasting. In *The Thirteenth International Conference on Learning Representations*, 2025.
- [36] Martin Andrae, Tomas Landelius, Joel Oskarsson, and Fredrik Lindsten. Continuous ensemble weather forecasting with diffusion models. In *The Thirteenth International Conference on Learning Representations*, 2025.
- [37] Hao Chen, Yunlong Yu, Yonghan Dong, Zheming Lu, Yingming Li, and Zhongfei Zhang. Multi-content interaction network for few-shot segmentation. *ACM Transactions on Multimedia Computing, Communications and Applications*, 20(6):1–20, 2024.
- [38] Boris Bonev, Thorsten Kurth, Christian Hundt, Jaideep Pathak, Maximilian Baust, Karthik Kashinath, and Anima Anandkumar. Spherical fourier neural operators: learning stable dynamics on the sphere. In *Proceedings of the 40th International Conference on Machine Learning*, 2023.
- [39] Wei Xiong, Muyuan Ma, Xiaomeng Huang, Ziyang Zhang, Pei Sun, and Yang Tian. Koopmanlab: machine learning for solving complex physics equations. *APL Machine Learning*, 1(3), 2023.
- [40] Zongyi Li, Nikola Borislavov Kovachki, Kamyar Azizzadenesheli, Burigede liu, Kaushik Bhattacharya, Andrew Stuart, and Anima Anandkumar. Fourier neural operator for parametric partial differential equations. In *International Conference on Learning Representations*, 2021.
- [41] Hao Chen, Tao Han, Jie Zhang, Song Guo, Fenghua Ling, and Lei Bai. Emformer: Efficient multi-scale transformer for accumulative context weather forecasting. In *International Conference on Machine Learning*, 2026.
- [42] Salva Rühling Cachay, Bo Zhao, Hailey Joren, and Rose Yu. Dyffusion: A dynamics-informed diffusion model for spatiotemporal forecasting. *Advances in neural information processing systems*, 36:45259–45287, 2023.
- [43] Lizao Li, Robert Carver, Ignacio Lopez-Gomez, Fei Sha, and John Anderson. Seeds: Emulation of weather forecast ensembles with diffusion models. *Science Advances*, 10:eadk4489, 2024.
- [44] Simon Lang, Mihai Alexe, Mariana CA Clare, Christopher Roberts, Rilwan Adewoyin, Zied Ben Bouallègue, Matthew Chantry, Jesper Dramsch, Peter D Dueben, Sara Hahner, et al. Aifs-crps: ensemble forecasting using a model trained with a loss function based on the continuous ranked probability score. *npj Artificial Intelligence*, 2(1):18, 2026.
- [45] Jaideep Pathak, Yair Cohen, Piyush Garg, Peter Harrington, Noah Brenowitz, Dale Durran, Morteza Mardani, Arash Vahdat, Shaoming Xu, Karthik Kashinath, et al. Kilometer-scale convection-allowing model emulation using generative diffusion modeling. *Science Advances*, 12(5):eadv0423, 2026.
- [46] Erik Larsson, Joel Oskarsson, Tomas Landelius, and Fredrik Lindsten. Diffusion-lam: probabilistic limited area weather forecasting with diffusion. *arXiv preprint arXiv:2502.07532*, 2025.
- [47] Tung Nguyen, Tuan Pham, Troy Arcomano, Rao Kotamarthi, Ian Foster, Sandeep Madireddy, and Aditya Grover. Omnicast: A masked latent diffusion model for weather forecasting across time scales. In *The Thirty-ninth Annual Conference on Neural Information Processing Systems*, 2025.
- [48] Donggeun Yoon, Minseok Seo, Doyi Kim, Yeji Choi, and Donghyeon Cho. Probabilistic weather forecasting with deterministic guidance-based diffusion model. In *Computer Vision – ECCV 2024*, pages 108–124, 2025.
- [49] Zhanxiang Hua, Yutong He, Chengqian Ma, and Alexandra Anderson-Frey. Weather prediction with diffusion guided by realistic forecast processes. *arXiv preprint arXiv:2402.06666*, 2024.
- [50] Salva Rühling Cachay, Brian Henn, Oliver Watt-Meyer, Christopher S. Bretherton, and Rose Yu. Probabilistic emulation of a global climate model with spherical Dyffusion. In *The Thirty-eighth Annual Conference on Neural Information Processing Systems*, 2024.
- [51] Jimeng Shi, Bowen Jin, Jiawei Han, Sundararaman Gopalakrishnan, and Giri Narasimhan. Codicast: Conditional diffusion model for global weather forecasting with uncertainty quantification. In *Proceedings of the Thirty-Fourth International Joint Conference on Artificial Intelligence, IJCAI-25*, pages 9853–9861, 8 2025.
- [52] Yi Xiao, Lei Bai, Wei Xue, Kang Chen, Tao Han, and Wanli Ouyang. Fengwu-4dvar: Coupling the data-driven weather forecasting model with 4d variational assimilation. *arXiv preprint arXiv:2312.12455*, 2023.
- [53] Kun Chen, Lei Bai, Fenghua Ling, Peng Ye, Tao Chen, Kang Chen, Tao Han, and Wanli Ouyang. Towards an end-to-end artificial intelligence driven global weather forecasting system. *arXiv preprint arXiv:2312.12462*, 2023.
- [54] Tao Han, Song Guo, Fenghua Ling, Kang Chen, Junchao Gong, Jingjia Luo, Junxia Gu, Kan Dai, Wanli Ouyang, and Lei Bai. Fengwu-ghr: Learning the kilometer-scale medium-range global weather forecasting. *arXiv preprint arXiv:2402.00059*, 2024.
- [55] Wanghan Xu, Kang Chen, Tao Han, Hao Chen, Wanli Ouyang, and Lei Bai. Extremecast: Boosting extreme value prediction for global weather forecast. *arXiv preprint arXiv:2402.01295*, 2024.
- [56] Dmitrii Kochkov, Janni Yuval, Ian Langmore, Peter Norgaard, Jamie Smith, Griffin Mooers, Milan Klöwer, James Lottes, Stephan Rasp, Peter Düben, et al. Neural general circulation models for weather and climate. *Nature*, 632(8027):1060–1066, 2024.
- [57] Cristian Bodnar, Wessel P Bruinsma, Ana Lucic, Megan Stanley, Anna Allen, Johannes Brandstetter, Patrick Garvan, Maik Riechert, Jonathan A Weyn, Haiyu Dong, et al. A foundation model for the earth system. *Nature*, 641(8065):1180–1187, 2025.

-
- [58] Johannes Schmude, Sujit Roy, Will Trojak, Johannes Jakubik, Daniel Salles Civitarese, Shraddha Singh, Julian Kuehnert, Kumar Ankur, Aman Gupta, Christopher E Phillips, et al. Prithvi wxc: Foundation model for weather and climate. *arXiv preprint arXiv:2409.13598*, 2024.
- [59] Simon Lang, Mihai Alexe, Matthew Chantry, Jesper Dramsch, Florian Pinault, Baudouin Raoult, Mariana CA Clare, Christian Lessig, Michael Maier-Gerber, Linus Magnusson, et al. Aifs-ecmwf’s data-driven forecasting system. *arXiv preprint arXiv:2406.01465*, 2024.
- [60] Simon Lang, Mihai Alexe, Mariana CA Clare, Christopher Roberts, Rilwan Adewoyin, Zied Ben Bouallègue, Matthew Chantry, Jesper Dramsch, Peter D Dueben, Sara Hahner, et al. Aifs-crps: Ensemble forecasting using a model trained with a loss function based on the continuous ranked probability score. *arXiv preprint arXiv:2412.15832*, 2024.
- [61] Kang Chen, Tao Han, Fenghua Ling, Junchao Gong, Lei Bai, Xinyu Wang, Jing-Jia Luo, Ben Fei, Wenlong Zhang, Xi Chen, et al. The operational medium-range deterministic weather forecasting can be extended beyond a 10-day lead time. *Communications Earth & Environment*, 6(1):518, 2025.
- [62] Sarah E Perkins and Lisa V Alexander. On the measurement of heat waves. *Journal of climate*, 26(13):4500–4517, 2013.
- [63] Daniel S Wilks. *Statistical methods in the atmospheric sciences*, volume 100. Academic press, 2011.

A Limitations

Although RealBench provides a more realistic benchmark for AI weather forecasting, several limitations remain. First, WEATHER-10K is based on globally distributed in-situ stations, but the station network is geographically imbalanced. Stations are denser in regions with well-developed meteorological infrastructure, such as North America, Europe, and parts of Asia, while coverage is sparser over oceans, deserts, high-latitude regions, and parts of Africa and South America. As a result, station-based evaluation may provide more reliable estimates in observation-dense regions than in sparsely observed regions.

Second, station observations and gridded analysis fields are not perfectly comparable because they represent different spatial scales. ERA5 and operational analysis data provide spatially complete and dynamically consistent atmospheric fields, whereas in-situ stations capture local surface conditions affected by terrain, land use, surface roughness, and boundary-layer processes. This scale mismatch is particularly important for near-surface variables and extreme events, and may lead to discrepancies that cannot be attributed solely to model forecast error.

Third, the evaluation of heatwaves and cold surges depends on the chosen event definition and matching protocol. Although the percentile-based threshold, consecutive-day criterion, and temporal-IoU matching strategy are designed to capture high-impact temperature extremes, the resulting scores may vary with the climatological baseline, threshold percentile, minimum event duration, and IoU threshold. Therefore, these metrics should be interpreted as one operationally motivated view of extreme-event skill rather than a unique definition of event predictability.

Finally, our benchmark evaluates existing data-driven forecasting systems under a unified protocol, but does not remove all differences among their native resolutions, input variables, training data, or operational adaptation. Tropical cyclone intensity prediction remains especially challenging: current AI models often capture storm tracks more reliably than storm intensity, and their intensity errors are affected by spatial resolution and smoothing of extreme pressure and wind structures. Future work should extend RealBench to additional years, more observation sources, probabilistic forecasts, and higher-resolution regional verification.

B Broader Impacts

RealBench has several positive societal implications. Accurate and reliable weather forecasting is important for many sectors, including aviation, maritime navigation, finance, energy, agriculture, disaster preparedness, and public safety. By evaluating AI weather models under operational conditions and against real-world station observations, RealBench can help researchers and practitioners better understand whether benchmark performance translates into real-world forecasting utility. Its explicit focus on high-impact events, including heatwaves, cold surges, and tropical cyclones, may support the development of more reliable forecasting systems for weather-risk mitigation and early warning.

At the same time, the benchmark should not be interpreted as a guarantee that any evaluated model is safe for direct operational deployment. Weather forecasts can influence high-stakes decisions, and incorrect predictions may lead to economic loss, inadequate preparation, or misplaced public trust. This is particularly important for extreme events, where our results show that current AI models may smooth temperature extremes, underperform on cold surges, or underestimate tropical cyclone intensity. Therefore, AI-based forecasts should be used with appropriate expert oversight, uncertainty communication, and comparison against established operational forecasting systems.

RealBench also highlights potential regional inequities in weather-model evaluation. Because in-situ station coverage is geographically imbalanced, station-based verification is more representative in observation-dense regions than in sparsely observed areas. Future benchmark development should incorporate additional observation sources and regional datasets to better assess forecasting performance in under-observed regions.

C Details of WEATHER-10K

C.1 Station Distribution and Country-level Statistics

Figure 6 summarizes the spatial distribution and country-level statistics of WEATHER-10K stations. WEATHER-10K contains 11,539 globally distributed surface weather stations, providing broad coverage over North America, Europe, East and South Asia, parts of South America, Africa, and Oceania. The station network is not spatially uniform: observations are denser in regions with well-developed meteorological infrastructure, especially the United States and Europe, while coverage is relatively sparse over deserts, high-latitude regions, oceans, and parts of Africa and South America. At the country level,

the United States contributes the largest number of stations, followed by ocean-based stations, Canada, Brazil, India, China, Kazakhstan, Spain, and several European and East Asian countries. This distribution reflects the heterogeneous availability of global in-situ observations and motivates evaluating forecasting models under realistic, irregularly distributed station coverage.

C.2 Data Preprocessing

We convert raw station observations into 6-hourly samples. For each target time t , we collect observations within a ± 15 minute window and average all valid records in the window:

$$y_{i,t}^v = \frac{1}{|O_{i,t}^v|} \sum_{\tau \in O_{i,t}^v} x_{i,\tau}^v, \quad O_{i,t}^v = \{\tau : |\tau - t| \leq 15 \text{ min}\}, \quad (4)$$

where $x_{i,\tau}^v$ denotes the raw observation of variable v at station i and time τ . Stations without valid observations in the window are excluded for that timestamp.

C.3 Quality Control with ERA5 Reference Fields

We further apply an ERA5-based quality-control step to remove extreme station outliers. For each 6-hourly timestamp, ERA5 single-level fields on a 0.25° grid are bilinearly interpolated to station locations. Temperature and dew-point temperature are converted from Kelvin to degrees Celsius, pressure variables from Pa to hPa, and ERA5 wind speed is computed from 10-meter wind components as $\sqrt{u_{10}^2 + v_{10}^2}$. We denote the processed station observation by $y_{i,t}^v$ and the corresponding station-interpolated ERA5 reference by $\hat{y}_{i,t}^v$. For temperature, dew-point temperature, station-level pressure, sea-level pressure, and wind speed, we flag an observation as anomalous if

$$\frac{y_{i,t}^v}{\hat{y}_{i,t}^v} > r_v, \quad (5)$$

where r_v is a variable-specific threshold. We use $r_v = 6$ for temperature and dew-point temperature, $r_v = 9000$ for sea-level pressure, and $r_v = 7$ for wind speed. Flagged values are replaced by the corresponding ERA5-interpolated values, while all other station observations are kept unchanged. This procedure removes severe physically implausible values while preserving the original in-situ observations whenever they pass the quality-control criterion.

D Additional Experimental Details

D.1 Baseline Models

All baseline models are widely recognized as strong data-driven numerical weather prediction systems, spanning graph-based, transformer-based, and hybrid architectures. For a fair comparison, we follow the official implementation and recommended inference protocol of each model. **The specific model checkpoints utilized for both ERA5-based and IFS-based (operational analysis) inference in this benchmark are summarized in Table 4.** We briefly introduce these baselines below.

AIFS [59] is the operational machine-learning forecasting system developed by ECMWF, which adopts a data-driven architecture trained on global reanalysis and operational analysis data to produce medium-range forecasts with competitive skill against numerical weather prediction systems. It is based on a graph neural network (GNN) encoder-decoder and a sliding-window transformer processor.

Aurora [57] is a large-scale foundation model for the atmosphere, trained on heterogeneous meteorological datasets and designed to support multiple forecasting tasks through a unified pretrained representation.

GraphCast [4] formulates global weather prediction as learning message passing on a multi-scale graph defined over the sphere, enabling efficient long-range information propagation while preserving the geometric structure of the Earth.

Pangu-Weather [8] employs a three-dimensional Earth-specific transformer architecture to model global atmospheric dynamics across pressure levels and surface variables, and produces forecasts in an autoregressive manner.

FuXi [13] is a cascade-based data-driven forecasting framework that uses separate neural networks for different lead-time ranges, improving medium-range prediction by reducing error accumulation over autoregressive rollouts.

FengWu [61] addresses global medium-range weather forecasting from a multi-modal and multi-task learning perspective, jointly modeling atmospheric variables and optimizing predictions across multiple lead times. It further incorporates a replay-buffer mechanism to enhance autoregressive forecasting skill at extended lead times.

Stormer [12] is a transformer-based global weather model that emphasizes scalable spatiotemporal representation learning for atmospheric states and supports efficient autoregressive forecasting.

NeuralGCM [56] combines differentiable general circulation modeling with learned neural parameterizations, representing a hybrid approach that integrates physical structure with data-driven components.

D.2 Complete List of Variables

Table 3 lists the input variables and vertical levels used by each baseline model during inference. The reported configuration corresponds to ERA5-based inference in our experiments. For operational analysis data, all baselines use the same input variables and levels as in the ERA5 setting, except GraphCast. GraphCast uses 37 pressure levels for ERA5 inference, namely 1, 2, 3, 5, 7, 10, 20, 30, 50, 70, 100, 125, 150, 175, 200, 225, 250, 300, 350, 400, 450, 500, 550, 600, 650, 700, 750, 775, 800, 825, 850, 875, 900, 925, 950, 975, and 1000 hPa, whereas it uses 13 pressure levels for operational analysis inference, namely 50, 100, 150, 200, 250, 300, 400, 500, 600, 700, 850, 925, and 1000 hPa. The surface variables used by GraphCast are identical in both settings.

D.3 Evaluation Metrics

We evaluate forecasts using four latitude-weighted metrics, including root-mean-square error (RMSE), anomaly correlation coefficient (ACC), bias, and activity, which account for varying grid-cell areas across latitudes and provide globally representative measures of forecast skill. Let $\hat{x}_t^v(i, j)$ and $x_t^v(i, j)$ denote the prediction and reference for variable v at lead time t and grid point (i, j) . We assign each latitude row a normalized area weight

$$w_i = \frac{N_{\text{lat}} \cos(\phi_i)}{\sum_{k=1}^{N_{\text{lat}}} \cos(\phi_k)}, \quad (6)$$

where ϕ_i is the latitude of row i . For simplicity, we use $\langle a \rangle_w = \frac{1}{N_{\text{lat}} N_{\text{lon}}} \sum_{i,j} w_i a(i, j)$ to denote the latitude-weighted spatial average.

The weighted RMSE measures the magnitude of forecast errors:

$$\text{RMSE}_t^v = \sqrt{\langle (\hat{x}_t^v - x_t^v)^2 \rangle_w}. \quad (7)$$

The weighted ACC measures the spatial correlation between forecast and reference anomalies relative to the climatological mean \bar{x}^v :

$$\text{ACC}_t^v = \frac{\langle (\hat{x}_t^v - \bar{x}^v) (x_t^v - \bar{x}^v) \rangle_w}{\sqrt{\langle (\hat{x}_t^v - \bar{x}^v)^2 \rangle_w} \sqrt{\langle (x_t^v - \bar{x}^v)^2 \rangle_w}}. \quad (8)$$

The weighted bias measures the signed mean forecast error:

$$\text{Bias}_t^v = \langle \hat{x}_t^v - x_t^v \rangle_w. \quad (9)$$

Finally, weighted activity measures the spatial variability of the predicted anomaly field:

$$\text{Activity}_t^v = \sqrt{\langle (\hat{x}_t^v - \bar{x}^v - \langle \hat{x}_t^v - \bar{x}^v \rangle_w)^2 \rangle_w}. \quad (10)$$

Power Spectra. The zonal energy spectrum measures the distribution of spatial variance across different physical scales (wavenumbers). For a given variable v at lead time t and latitude row i , the discrete Fourier transform (DFT) along the longitudinal dimension j is:

$$F_{t,k}^v(i) = \frac{1}{N_{\text{lon}}} \sum_{j=0}^{N_{\text{lon}}-1} \hat{x}_t^v(i, j) e^{-i2\pi k j / N_{\text{lon}}}, \quad (11)$$

where k is the zonal wavenumber. The energy spectrum is then computed as:

$$S_{t,0}^v(i) = C_i |F_{t,0}^v(i)|^2, \quad S_{t,k}^v(i) = 2C_i |F_{t,k}^v(i)|^2 \quad \text{for } k > 0, \quad (12)$$

where $C_i = 2\pi R \cos(\phi_i)$ is the physical circumference of latitude ϕ_i (R is the Earth’s radius). The factor of 2 ensures energy conservation by accounting for negative frequencies. Finally, the representative spectrum for active weather systems is obtained by averaging $S_{t,k}^v(i)$ over the mid-latitudes ($30^\circ < |\phi_i| < 60^\circ$).

All metrics are computed independently for each evaluated variable and forecast lead time.

Temperature Extreme Event Definition and Matching. For temperature extremes, let $T_{y,t}(x)$ denote the 2m temperature at location x and time t in year y . We define the daily maximum and minimum 2m temperature as

$$T_{y,c}^{\max}(x) = \max_{t \in c} T_{y,t}(x), \quad T_{y,c}^{\min}(x) = \min_{t \in c} T_{y,t}(x), \quad (13)$$

where c denotes a calendar day and $t \in c$ indexes all time steps within that day. For each calendar day, we construct a 15-day moving climatological window $\mathcal{W}_c = \{c-7, \dots, c+7\}$ using 12 years of historical data $\mathcal{Y}_{\text{hist}}$. This 12-year baseline is adopted in place of the standard 30-year climatology to balance computational efficiency with the constraints of our available historical dataset. The heatwave and cold surge thresholds are defined as the 90th and 10th percentiles [62], respectively:

$$\tau_c^H(x) = Q_{0.9} \left(\left\{ T_{y,c'}^{\max}(x) : y \in \mathcal{Y}_{\text{hist}}, c' \in \mathcal{W}_c \right\} \right), \quad (14)$$

$$\tau_c^C(x) = Q_{0.1} \left(\left\{ T_{y,c'}^{\min}(x) : y \in \mathcal{Y}_{\text{hist}}, c' \in \mathcal{W}_c \right\} \right). \quad (15)$$

A heat-wave event is identified when the daily maximum temperature exceeds the corresponding threshold for at least three consecutive days; analogously, a cold surge event is identified when the daily minimum temperature falls below the corresponding threshold for at least three consecutive days. Specifically, for a three-day interval starting at day c , the binary event labels are

$$E_{y,c}^H(x) = \prod_{\delta=0}^2 \mathbf{1} \left[T_{y,c+\delta}^{\max}(x) > \tau_{c+\delta}^H(x) \right], \quad E_{y,c}^C(x) = \prod_{\delta=0}^2 \mathbf{1} \left[T_{y,c+\delta}^{\min}(x) < \tau_{c+\delta}^C(x) \right]. \quad (16)$$

We compute the above binary event labels for both forecasts and ground truth. To account for small temporal displacement errors in predicted events, we match predicted and ground-truth events using the intersection-over-union (IoU) criterion. For a predicted event \hat{E} and a ground-truth event E , the IoU is defined as

$$\text{IoU}(\hat{E}, E) = \frac{|\hat{E} \cap E|}{|\hat{E} \cup E|}, \quad (17)$$

where $|\hat{E} \cap E|$ and $|\hat{E} \cup E|$ denote the number of overlapping and union event days, respectively. A predicted event is considered a true positive if it can be matched to a ground-truth event with

$$\text{IoU}(\hat{E}, E) \geq \gamma, \quad (18)$$

where $\gamma = 0.5$ unless otherwise specified. Each ground-truth event is matched to at most one prediction. Unmatched predicted events are counted as false positives, and unmatched ground-truth events are counted as false negatives.

D.4 Implementation Details

We implement all inference baselines in a unified evaluation pipeline and report efficiency under a fixed operational protocol. Specifically, we evaluate one full year (365 days), with 4 initialization times per day, and 40 forecast updates per initialization (6-hour cadence), resulting in 58,400 forecast updates per model for the sequential-throughput estimate. Unless otherwise stated, efficiency is measured with batch size set to 1, and we report parameter count, per-step inference latency (after warmup), peak GPU memory, and estimated total sequential GPU hours for the full protocol.

For NeuralGCM, we follow its native temporal integration setting and account for its 1-hour internal timestep when estimating long-horizon runtime, so that comparisons are aligned by forecast horizon rather than by internal step count. All experiments are conducted on our production compute cluster with multi-GPU nodes; each model is benchmarked on a single GPU process at a time, and multi-GPU parallelism is used only for throughput scaling across independent runs. The complete efficiency results are summarized in Table 5.

Experiments are conducted on a server with 2× Intel Xeon Platinum 8457C CPUs and 8× NVIDIA H20 GPUs (97,871 MiB per GPU, driver 535.161.08).

D.5 More Experimental Results

Additional Overall Evaluation Results. Figures 7, 8, 9, 10, and 12 present the evolution of WRMSE, Bias, and Activity as functions of forecast lead time for different data-driven weather forecasting models. The metrics are evaluated on ERA5 reanalysis data, operational analysis data, and WEATHER-10K station observations, providing a comprehensive comparison of forecast accuracy, systematic bias, and variability preservation across multiple evaluation datasets.

Figure 11 shows zonal-mean power spectra for four variables (Z500, Q700, U850, and T2M) at lead times of 6 h, 3 d, 5 d, and 10 d. The ERA5 curve is invariant across lead times and serves as a common reference. Overall, most models are closer to ERA5 at low wavenumbers (large scales), while larger deviations appear at high wavenumbers (small scales). From 6 h to 10 d, high-wavenumber deviations increase for several variables. By variable, Q700 and T2M show more pronounced differences at the high-wavenumber end, U850 remains more consistent in the low-to-mid wavenumber range, and Z500 exhibits larger inter-model spread in the spectral tail. Distinct local peaks and wiggles are also visible at high wavenumbers for some models. NeuralGCM is reported only for upper-air variables (Z500/Q700/U850), and is not shown for T2M.

Global Visualizations. Figures 13, 14, 15, and 16 show global visualizations of near-surface and upper-air forecasts produced by data-driven weather forecasting models. The forecasts are initialized from ERA5 and operational analysis data at 00:00 UTC on July 10, 2025, and the results at a lead time of 10 days are presented to illustrate the large-scale spatial structures and forecast behaviors across different atmospheric variables.

Additional Tropical Cyclone Results. Figure 17 reports lead-time-dependent track errors for all seven models under ERA5 and IFS initialization. For all models, errors increase with lead time. Differences among models are small at short leads and become larger at medium-to-long leads. The relative ordering is broadly similar across the two initialization settings, while the error spread is more visible after longer lead times.

Figures 18, 19, and 20 provide three representative event-level tropical cyclone evaluations (Danas, Matmo, and Ragasa) under a unified protocol. For each event, panels (a) and (b) show forecast tracks initialized from ERA5 and IFS, respectively, against the IBTrACS reference track, and panel (c) reports model-wise track error as a function of lead time (0–120 h). Across the three cases, near-initial lead errors are generally smaller and become larger at later leads, while the spread among models is limited at short leads and more pronounced at medium-to-long leads. The degree of spread and the ordering among models vary by event, indicating clear case dependence in track behavior. Overall, these case studies are consistent with the aggregate statistics in the main benchmark and serve as supplementary, event-wise evidence of inter-model differences under the same data window and evaluation settings (June to December 2025).

Additional Case-Based Results for Extreme Temperature Events. Figures 21 and 22 report case-based results for three heatwave events and three cold-surge events in the second half of 2025. Each figure uses the same three-panel layout: (i) peak-day ERA5 temperature field with an object-based event boundary and analysis box, (ii) area-averaged temperature time series at 3-day lead, and (iii) lead-time-dependent bias (1, 3, 7, and 10 days) averaged over the event core period.

From the heatwave cases, two consistent observations are visible. First, agreement with ERA5 is generally higher at short lead times than at longer lead times. Second, several models show increasingly negative T_{max} bias at longer leads in the strongest events, indicating reduced peak-intensity fidelity as lead time increases.

From the cold-surge cases, a parallel pattern is observed. Model spread increases with lead time, and positive T_{min} bias becomes more common at longer leads, corresponding to weaker simulated cold intensity relative to ERA5. The magnitude of this behavior is case-dependent across regions.

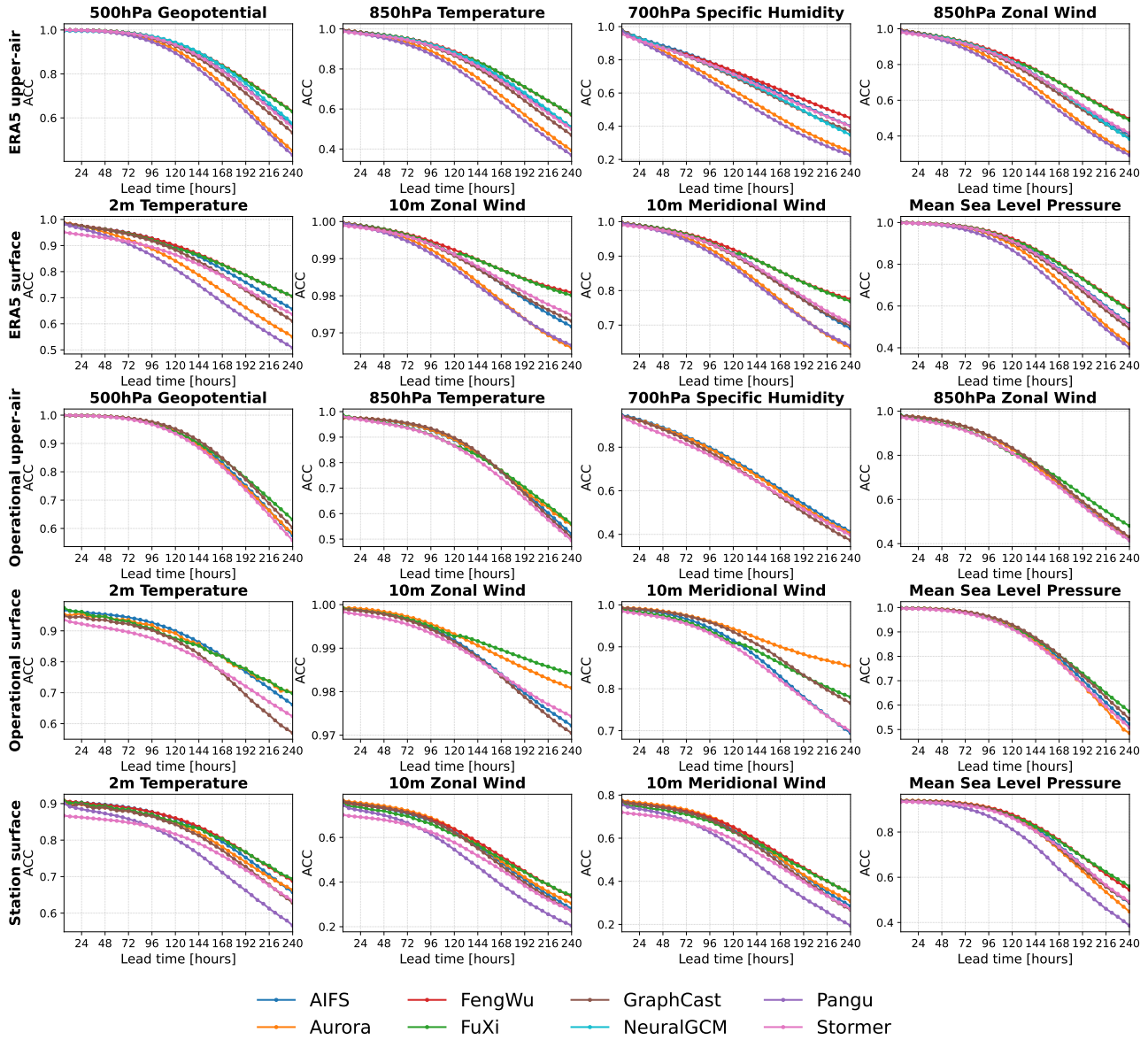


Figure 5. ACC \uparrow comparison of eight baseline models across ERA5, operational analysis data, and WEATHER-10K station evaluations in global weather forecasting.

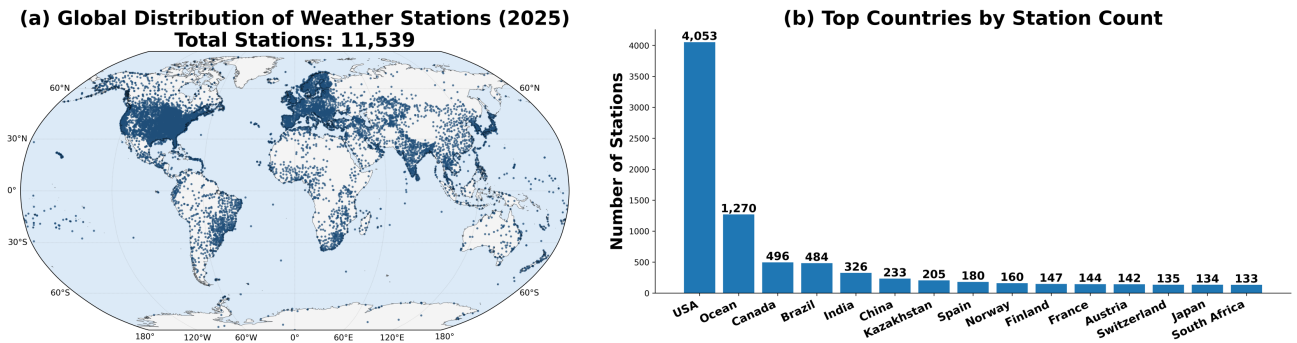


Figure 6. Station distribution of WEATHER-10K. (a) Global locations of all 11,539 stations, showing dense coverage over North America, Europe, and parts of Asia, and relatively sparse coverage over oceans, deserts, high-latitude regions, and parts of Africa and South America. (b) Top countries or regions by station count.

Model	Input variables	Vertical levels
AIFS	Pressure-level variables: geopotential (Z), specific humidity (Q), temperature (T), zonal wind (U), meridional wind (V), vertical velocity (W). Single-level variables: 2m temperature (T2M), 10m zonal wind (U10), 10m meridional wind (V10), mean sea-level pressure (MSL), surface pressure (SP), total column water (TCW), skin temperature (SKT), 2m dewpoint temperature (D2M), total precipitation (TP), convective precipitation (CP), land-sea mask (LSM), standard deviation of sub-grid orography (SDOR), slope of sub-grid orography (SLOR), total cloud cover (TCC), geopotential at surface (Z), soil temperature level 1 (STL1), soil temperature level 2 (STL2), volumetric soil water layer 1 (SWVL1), volumetric soil water layer 2 (SWVL2).	Pressure levels: 50, 100, 150, 200, 250, 300, 400, 500, 600, 700, 850, 925, 1000 hPa.
Aurora	Pressure-level variables: geopotential (Z), specific humidity (Q), temperature (T), zonal wind (U), meridional wind (V). Surface variables: mean sea-level pressure (MSL), 10m zonal wind (U10), 10m meridional wind (V10), 2m temperature (T2M).	Pressure levels: 50, 100, 150, 200, 250, 300, 400, 500, 600, 700, 850, 925, 1000 hPa.
GraphCast	Pressure-level variables: geopotential (Z), specific humidity (Q), temperature (T), zonal wind (U), meridional wind (V), vertical velocity (W). Surface variables: mean sea-level pressure (MSL), 10m zonal wind (U10), 10m meridional wind (V10), 2m temperature (T2M), 6-hour accumulated total precipitation (TP6H).	Pressure levels: 1, 2, 3, 5, 7, 10, 20, 30, 50, 70, 100, 125, 150, 175, 200, 225, 250, 300, 350, 400, 450, 500, 550, 600, 650, 700, 750, 775, 800, 825, 850, 875, 900, 925, 950, 975, 1000 hPa.
Pangu-Weather	Pressure-level variables: geopotential (Z), specific humidity (Q), temperature (T), zonal wind (U), meridional wind (V). Surface variables: mean sea-level pressure (MSL), 10m zonal wind (U10), 10m meridional wind (V10), 2m temperature (T2M).	Pressure levels: 50, 100, 150, 200, 250, 300, 400, 500, 600, 700, 850, 925, 1000 hPa.
FengWu	Pressure-level variables: geopotential (Z), specific humidity (Q), temperature (T), zonal wind (U), meridional wind (V). Surface variables: mean sea-level pressure (MSL), 10m zonal wind (U10), 10m meridional wind (V10), 2m temperature (T2M).	Pressure levels: 50, 100, 150, 200, 250, 300, 400, 500, 600, 700, 850, 925, 1000 hPa.
FuXi	Pressure-level variables: geopotential (Z), temperature (T), zonal wind (U), meridional wind (V), relative humidity (R). Surface variables: 2m temperature (T2M), 10m zonal wind (U10), 10m meridional wind (V10), mean sea-level pressure (MSL), 6-hour accumulated total precipitation (TP6H).	Pressure levels: 50, 100, 150, 200, 250, 300, 400, 500, 600, 700, 850, 925, 1000 hPa.
Stormer	Pressure-level variables: geopotential (Z), specific humidity (Q), temperature (T), zonal wind (U), meridional wind (V). Surface variables: mean sea-level pressure (MSL), 10m zonal wind (U10), 10m meridional wind (V10), 2m temperature (T2M).	Pressure levels: 50, 100, 150, 200, 250, 300, 400, 500, 600, 700, 850, 925, 1000 hPa.
NeuralGCM	Pressure-level variables: geopotential (Z), specific humidity (Q), temperature (T), zonal wind (U), meridional wind (V), specific cloud ice water content (CIWC), specific cloud liquid water content (CLWC). Surface forcings: sea-surface temperature (SST), sea-ice concentration (SICONC).	Pressure levels: 1, 2, 3, 5, 7, 10, 20, 30, 50, 70, 100, 125, 150, 175, 200, 225, 250, 300, 350, 400, 450, 500, 550, 600, 650, 700, 750, 775, 800, 825, 850, 875, 900, 925, 950, 975, 1000 hPa.

Table 3. Input variables and vertical levels used by different baseline models during ERA5-based inference.

Model	ERA5 checkpoint	IFS checkpoint	Source
AIFS	aifs-single-mse-1.1.ckpt	aifs-single-mse-1.1.ckpt	https://huggingface.co/ecmwf/aifs-single-1.1
Aurora	aurora-0.25-pretrained.ckpt	aurora-0.25-finetuned.ckpt	https://huggingface.co/microsoft/aurora
GraphCast	GraphCast-ERA51979-2017-resolution0.25-pressurelevels37-mesh2to6-precipitationinputandoutput.npz	—	https://github.com/google-deepmind/graphcast
GraphCast (operational)	—	GraphCast_operational-ERA5-HRES1979-2021-resolution0.25-pressurelevels13-mesh2to6-precipitationoutputonly.npz	https://github.com/google-deepmind/graphcast
Pangu-Weather	pangu_weather_6.onnx	pangu_weather_6.onnx	https://github.com/198808xc/Pangu-Weather
FengWu	fengwu_v1.onnx	fengwu_v2.onnx	https://github.com/OpenEarthLab/FengWu
FuXi	short.onnx, medium.onnx, long.onnx	short.onnx, medium.onnx, long.onnx	https://github.com/tpys/FuXi
Stormer	stormer_1.40625_patch_size_2.ckpt	stormer_1.40625_patch_size_2.ckpt	https://github.com/tung-nd/stormer
NeuralGCM	models_v1_deterministic_0_7_deg.pkl	—	https://github.com/google-research/neuralgcm

Table 4. Model checkpoints used for ERA5-based and IFS-based inference in this benchmark.

	Pangu	Stormer	FengWu	FuXi	AIFS	GraphCast	NeuralGCM
Total time (h)	12.1	10.6	20.8	19.5	10.1	14.3	92.9
GPU (MiB)	12,387	15,141	17,507	5,815	20,465	73,753	73,777
Params (M)	276.7	468.8	427.4	1563.3	253.0	36.5	31.1

Table 5. Efficiency comparison of seven data-driven weather forecasting models. All statistics are evaluated with batch size = 1, including total inference time, GPU memory consumption, and the number of model parameters.

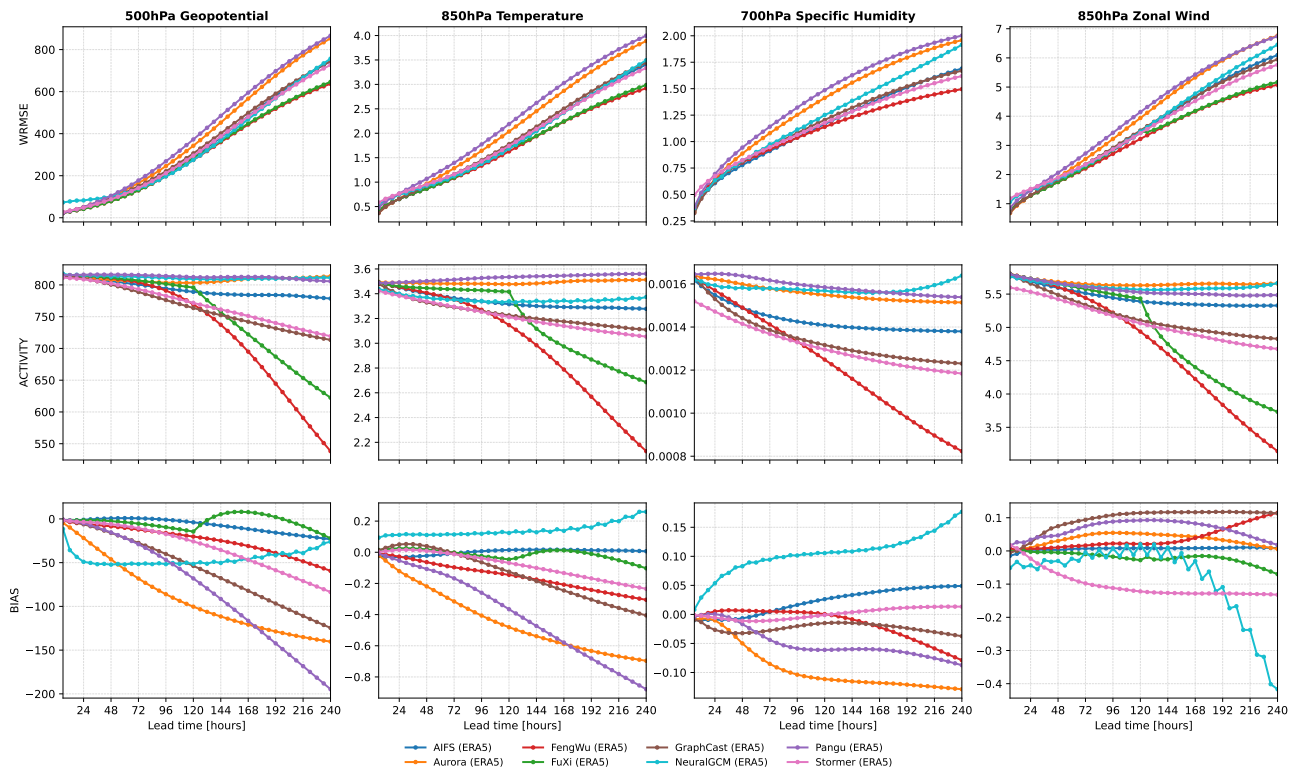


Figure 7. WRMSE ↓, Activity ↑, and Bias comparisons of eight baseline models for upper-air variables across ERA5 evaluations in global weather forecasting.

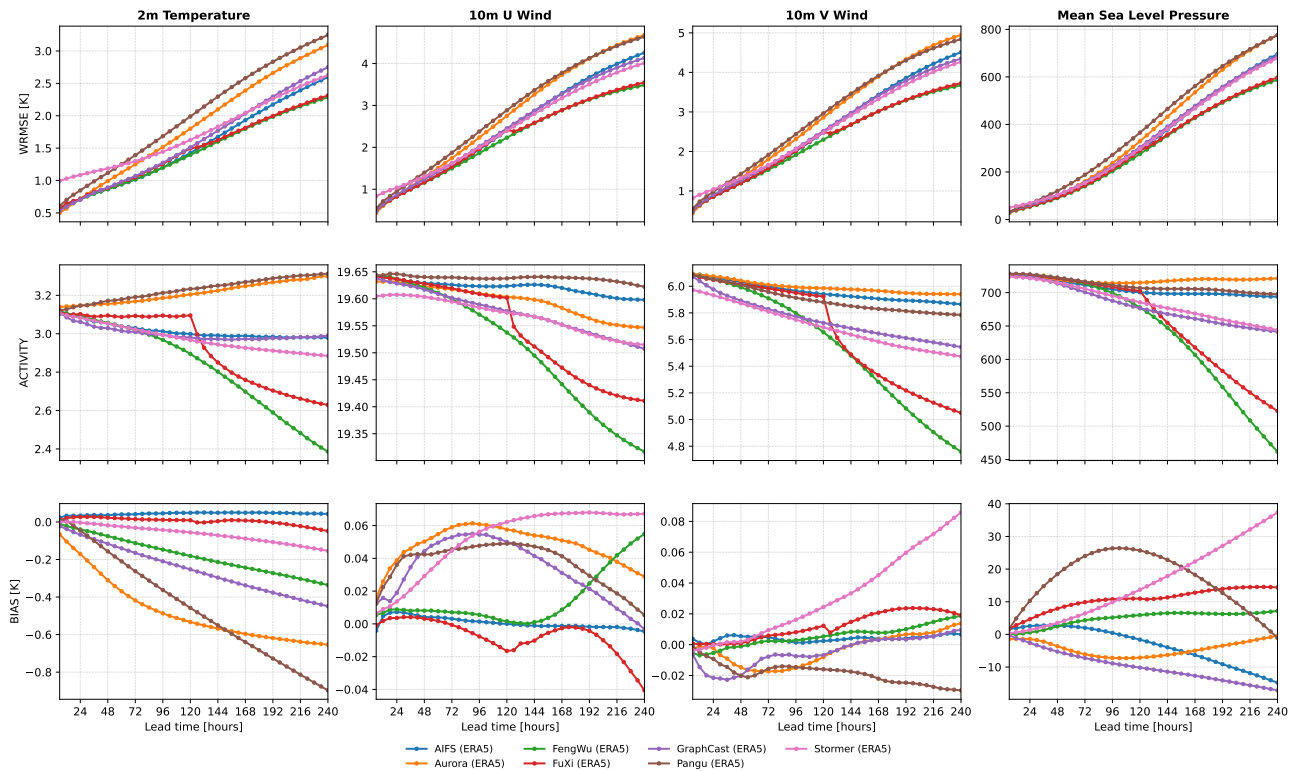


Figure 8. WRMSE ↓, Activity ↑, and Bias comparisons of eight baseline models for surface variables across ERA5 evaluations in global weather forecasting.

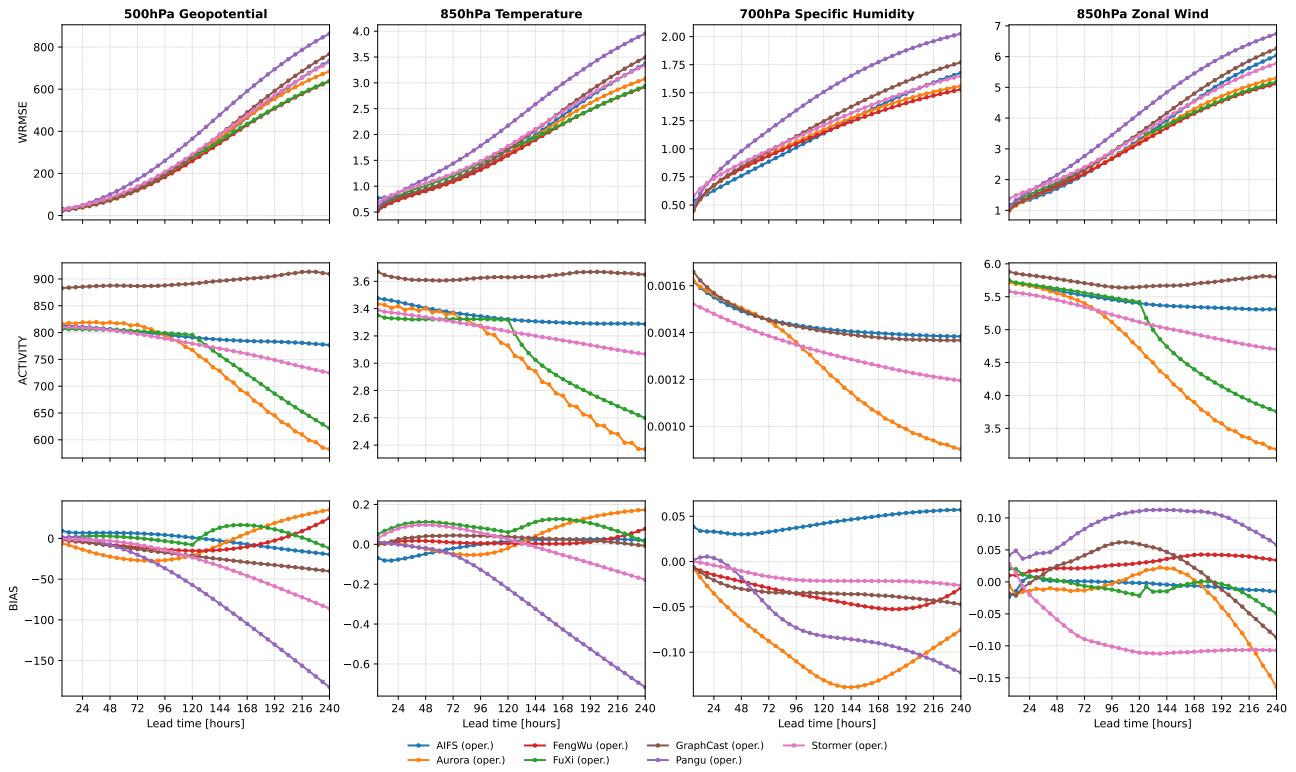


Figure 9. WRMSE ↓, Activity ↑, and Bias comparisons of eight baseline models for upper-air variables across operational analysis data evaluations in global weather forecasting.

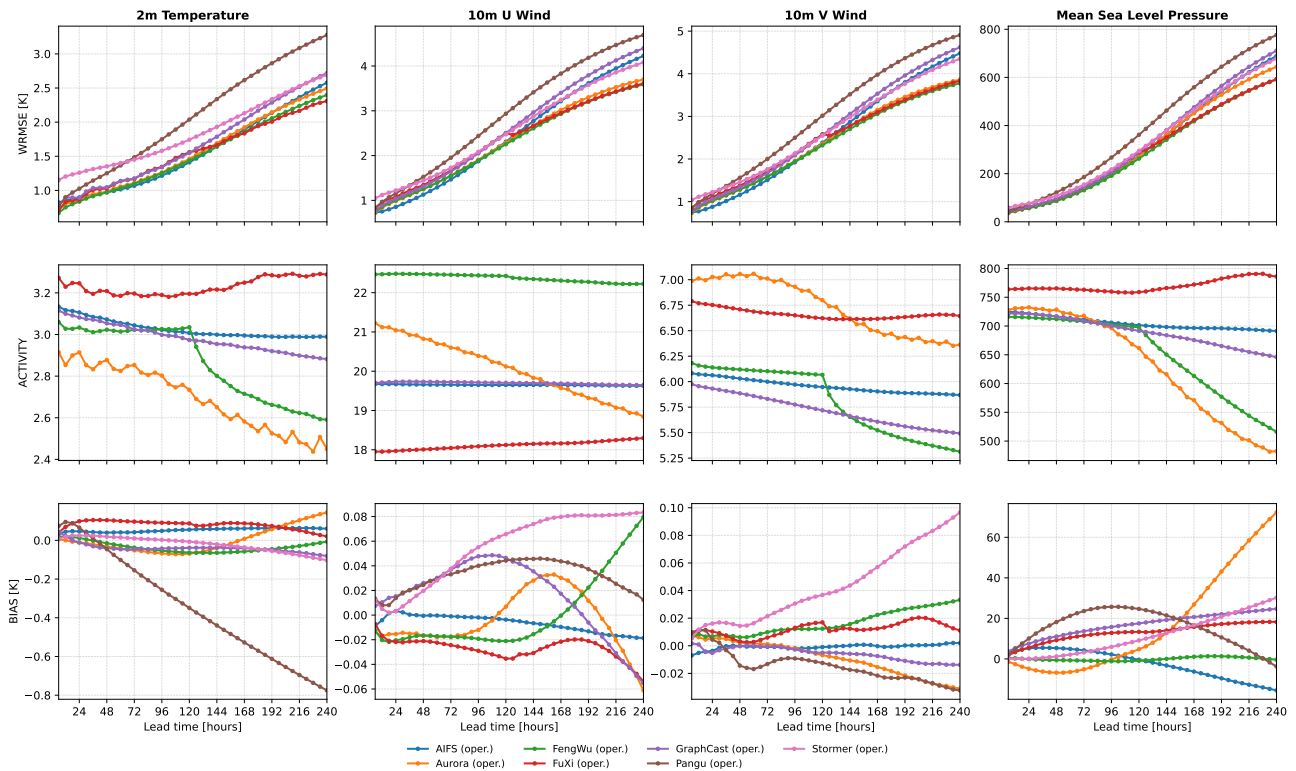


Figure 10. WRMSE ↓, Activity ↑, and Bias comparisons of eight baseline models for surface variables across operational analysis data evaluations in global weather forecasting.

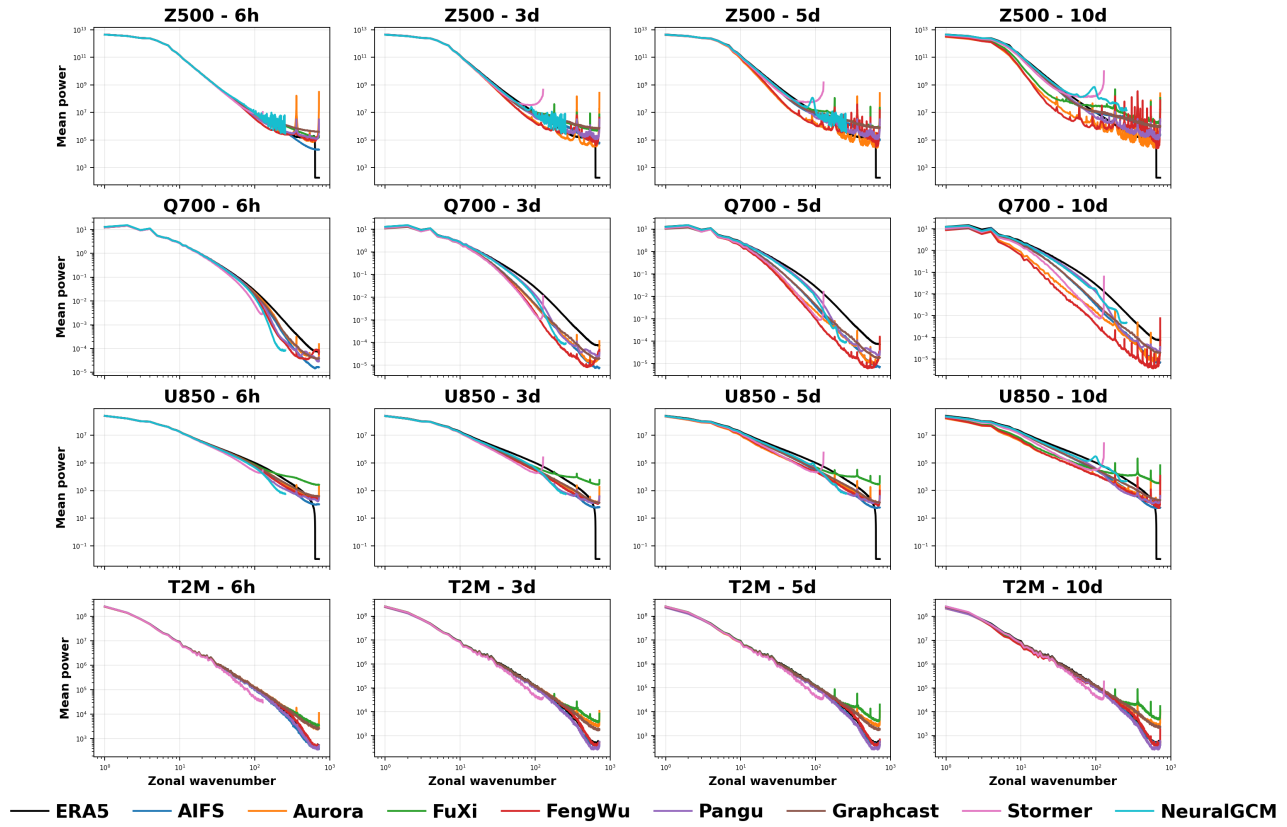


Figure 11. Zonal-mean power spectra for 500 hPa geopotential, 700 hPa specific humidity, 850 hPa zonal wind, and 2 m temperature at leads of 6 h, 3 d, 5 d, and 10 d. Multiple AI models are compared against ERA5 (black)

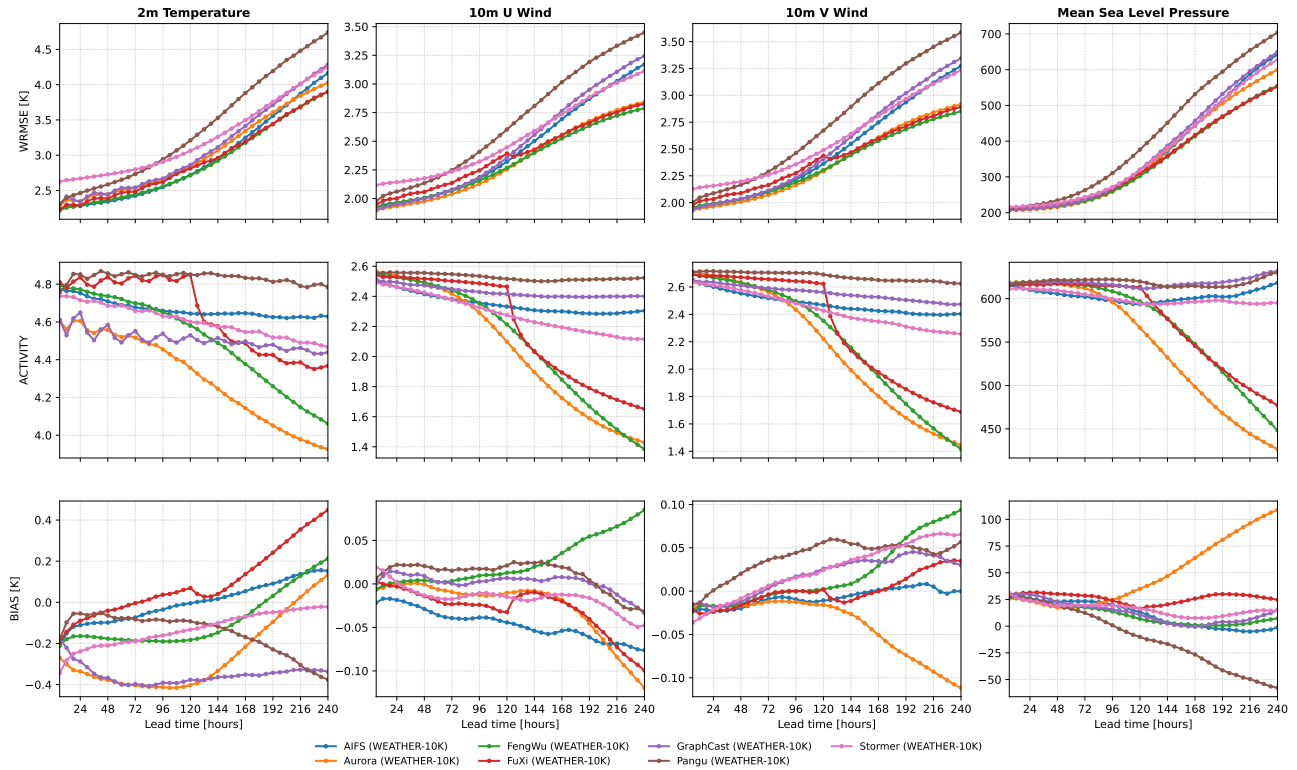


Figure 12. WRMSE ↓, Activity ↑, and Bias comparisons of eight baseline models for surface variables across WEATHER-10K evaluations in global weather forecasting.

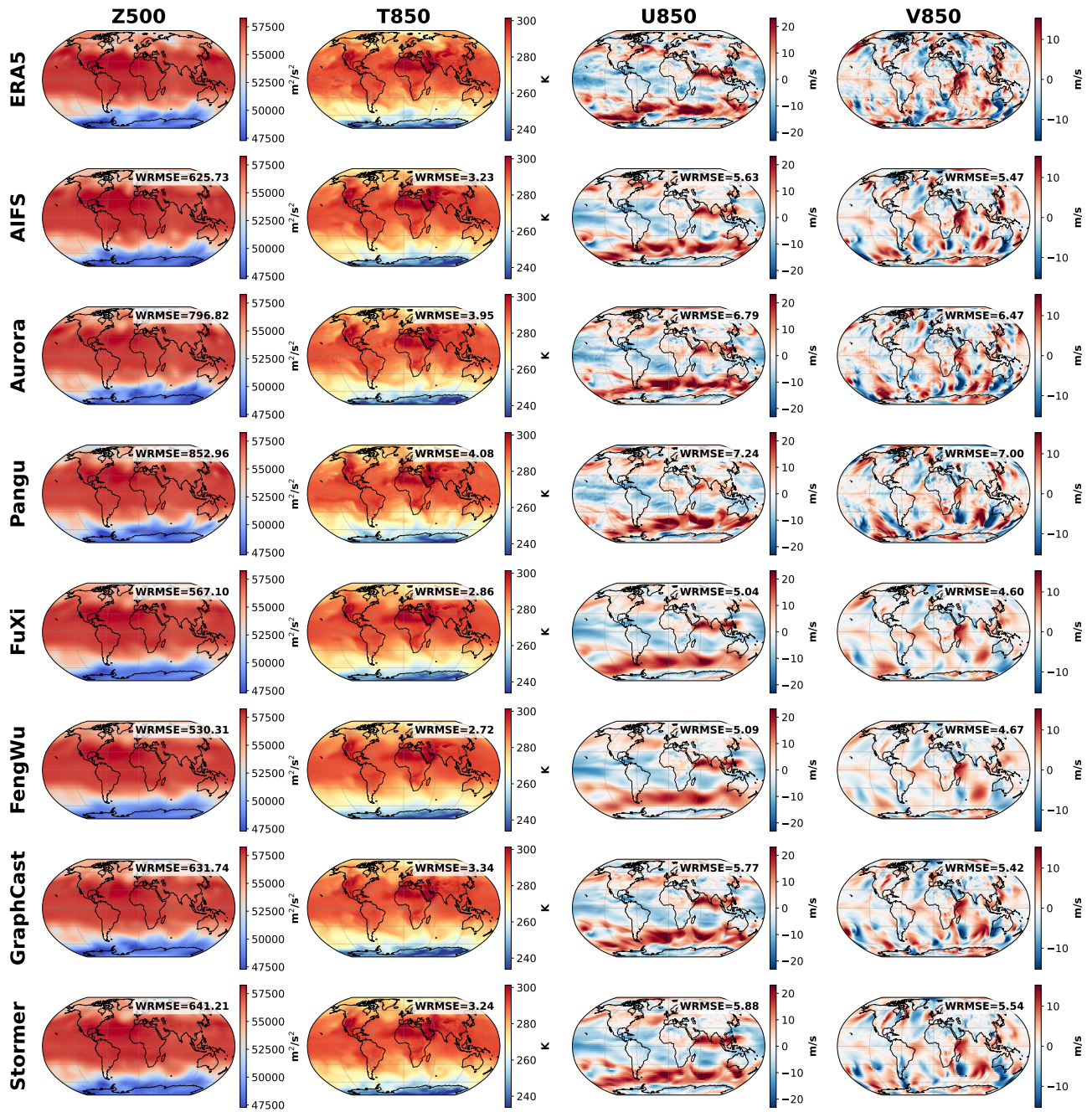


Figure 13. Visualization of 10-day global forecasts for upper-air variables generated by data-driven weather forecasting models, initialized at 00:00 UTC on July 10, 2025, with inference performed on ERA5.

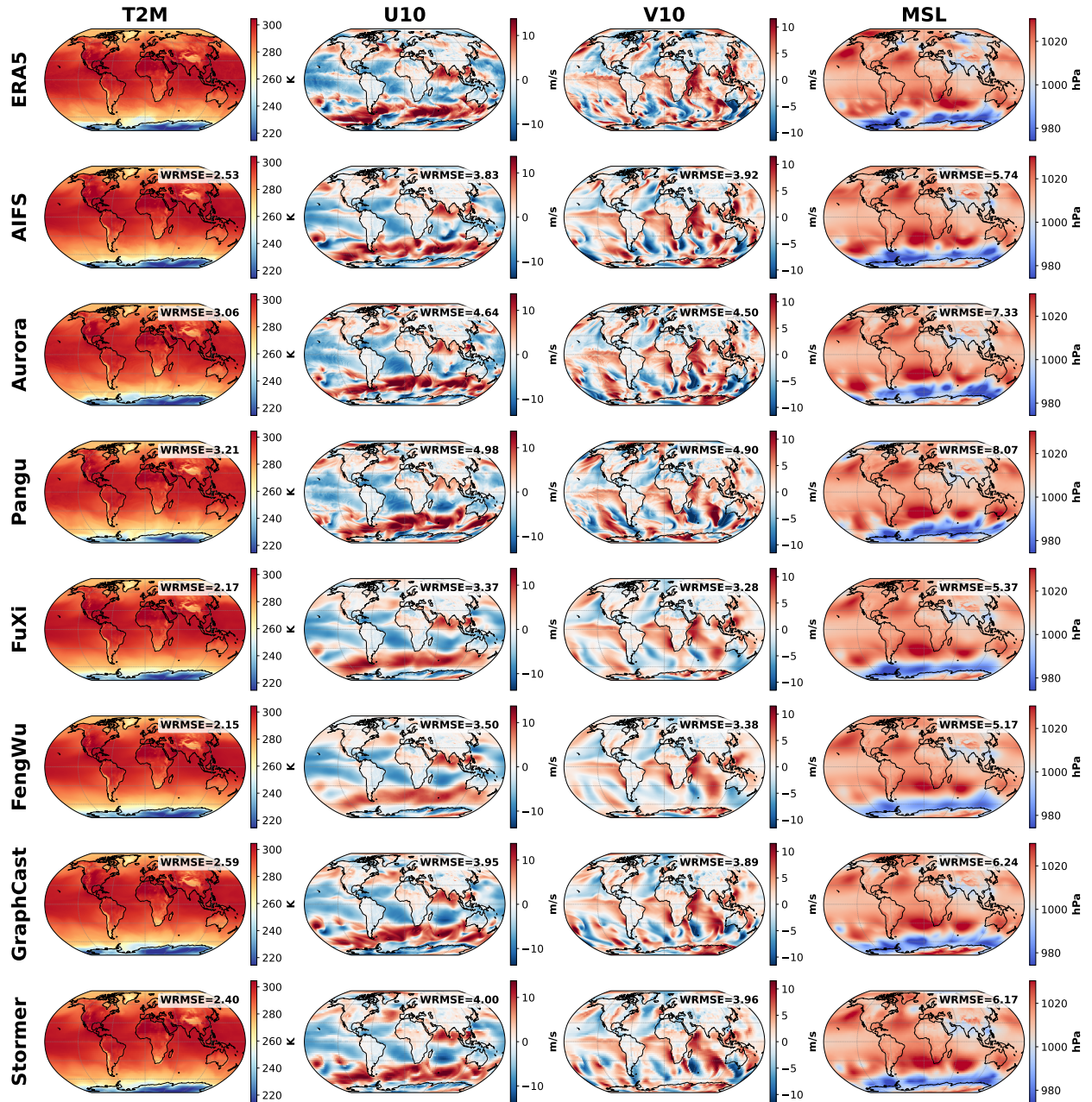


Figure 14. Visualization of 10-day global forecasts for surface variables generated by data-driven weather forecasting models, initialized at 00:00 UTC on July 10, 2025, with inference performed on ERA5.

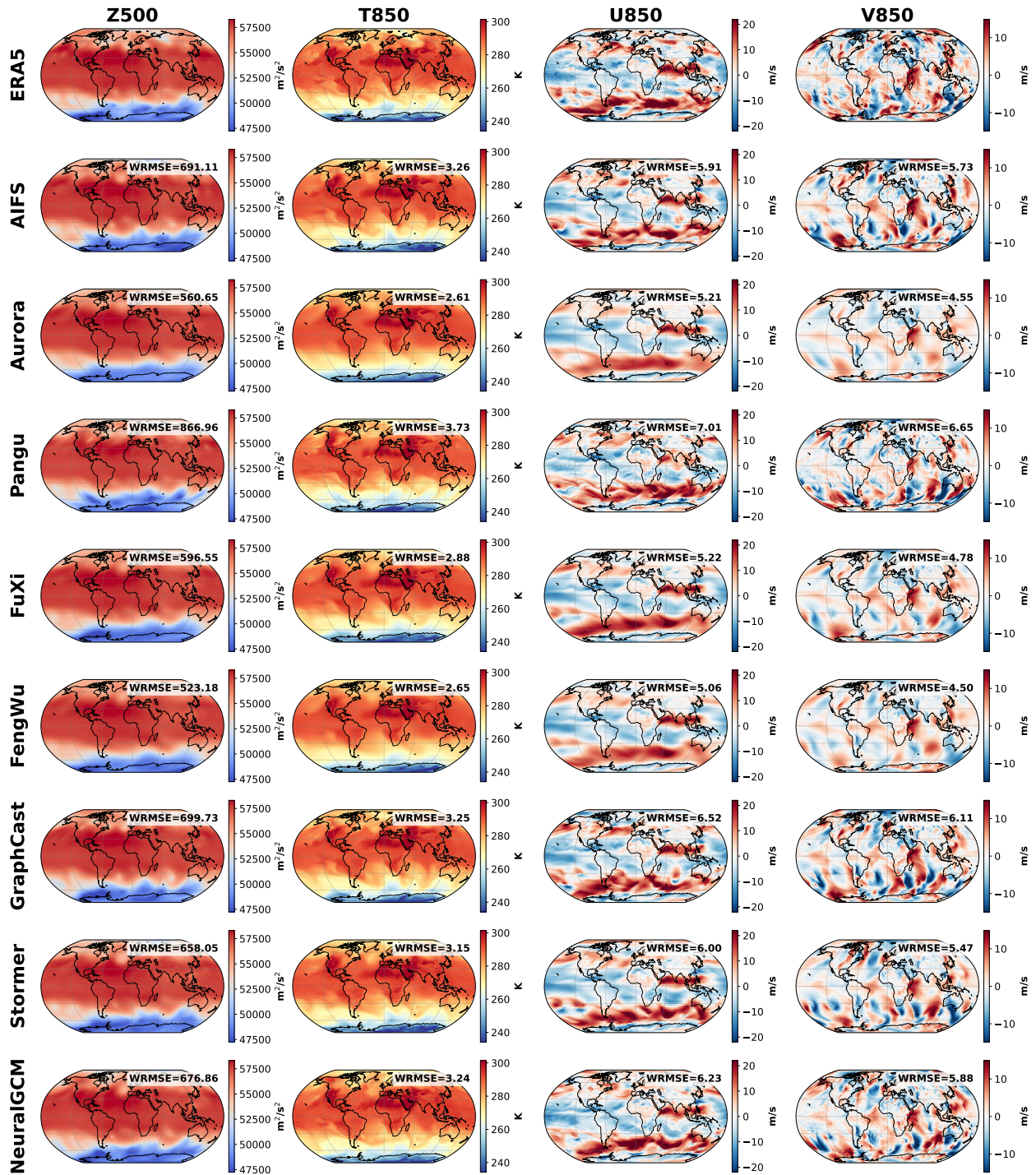


Figure 15. Visualization of 10-day global forecasts for upper-air variables generated by data-driven weather forecasting models, initialized at 00:00 UTC on July 10, 2025, with inference performed on operational analysis data.

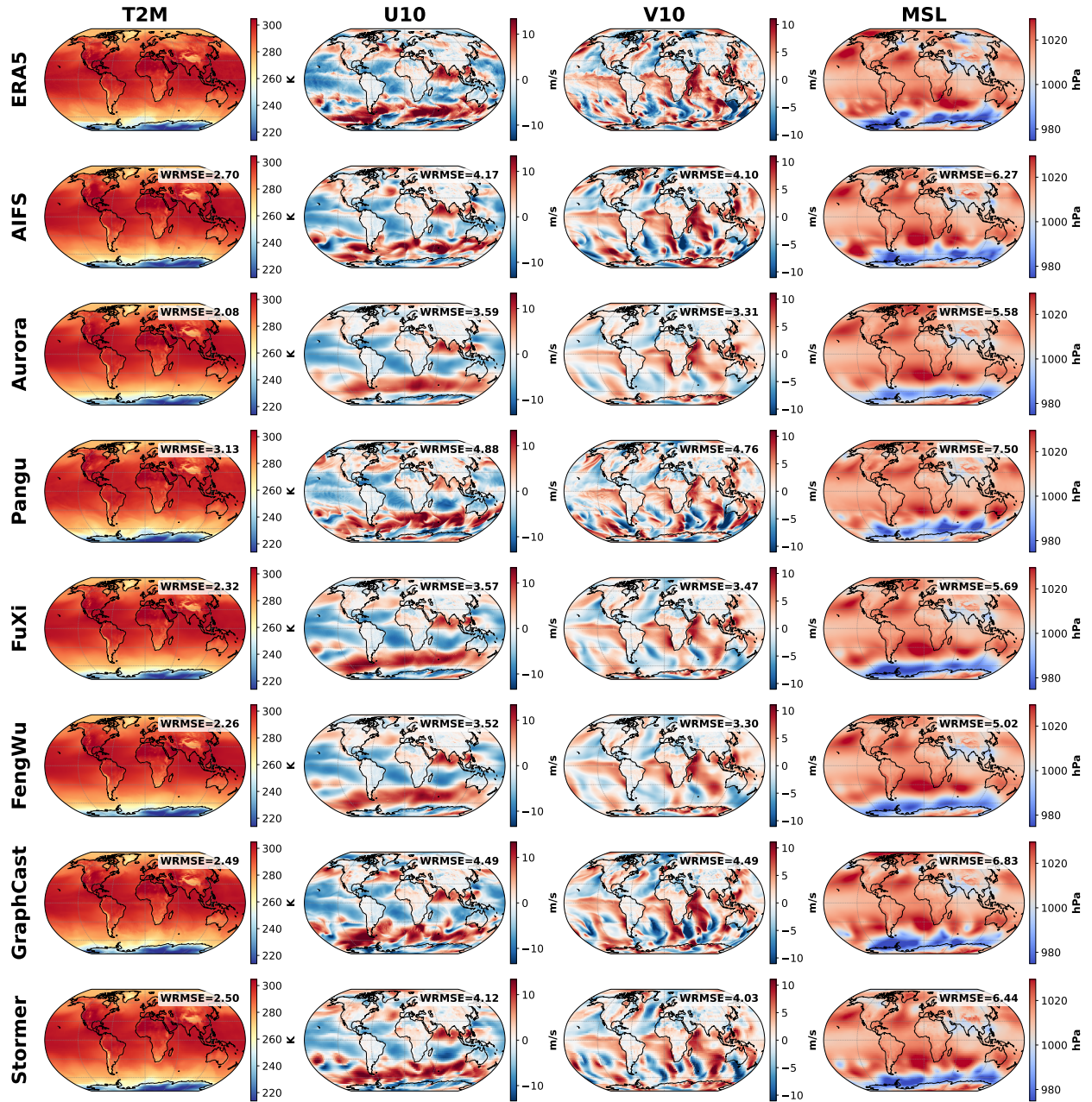


Figure 16. Visualization of 10-day global forecasts for surface variables generated by data-driven weather forecasting models, initialized at 00:00 UTC on July 10, 2025, with inference performed on operational analysis data.

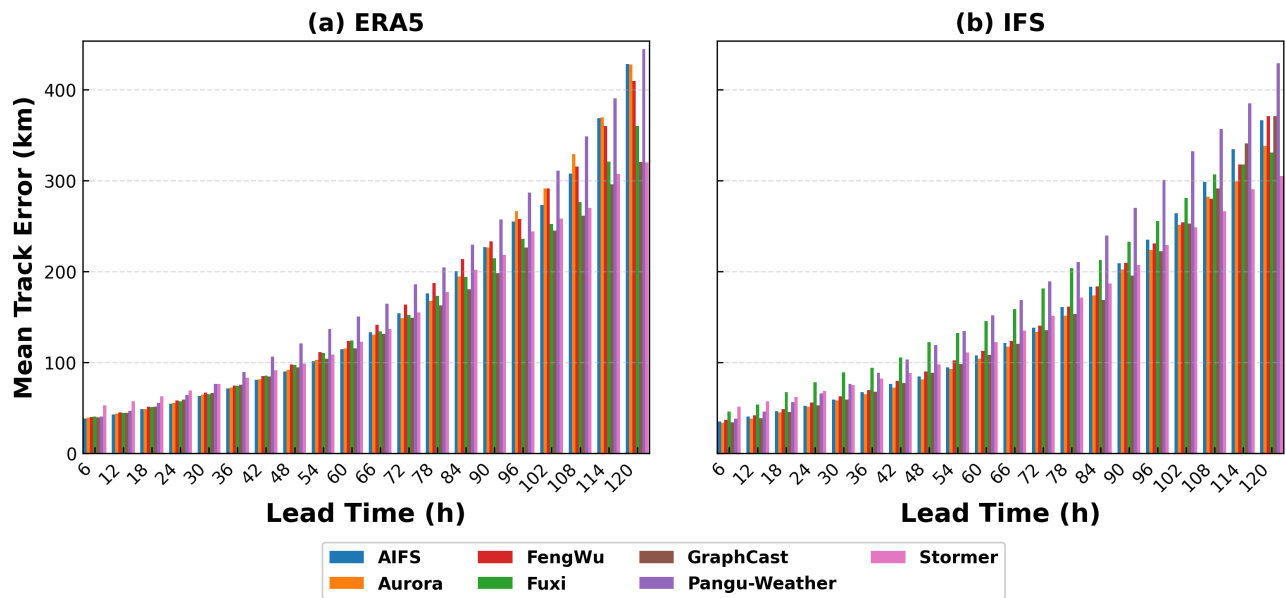


Figure 17. Mean tropical cyclone track error (km) versus lead time (6–120 h) from June to December 2025 for seven AI weather models, comparing ERA5-initialized and IFS-initialized forecasts.

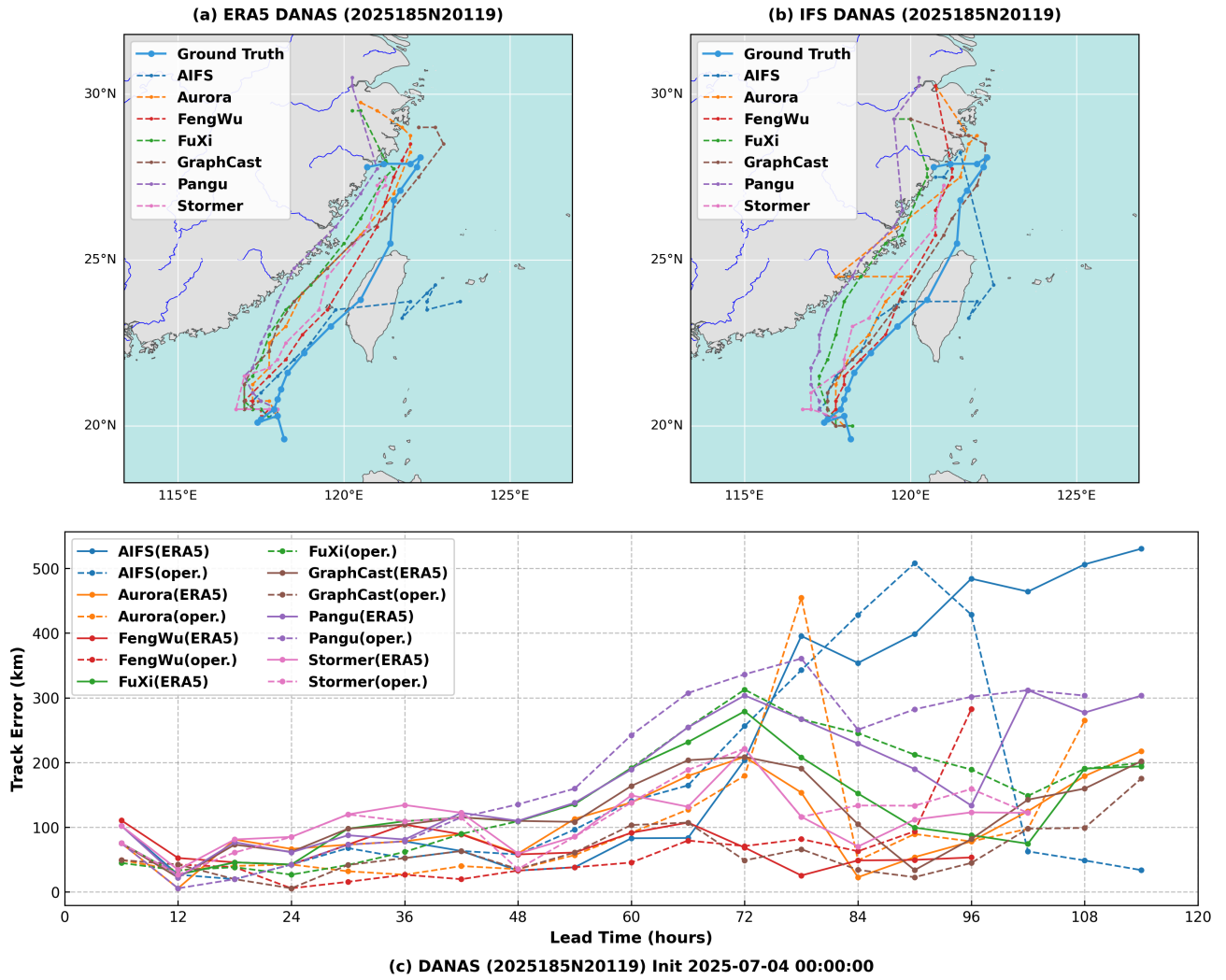


Figure 18. Track forecasts initialized from (a) ERA5 and (b) IFS analysis for Typhoon Danas (IBTrACS ID 2025185N20119; initialization 0000 UTC 4 July 2025). Observed track from IBTrACS (blue). (c) Mean-distance track error versus lead time (0–120 h) for each model and initialization.

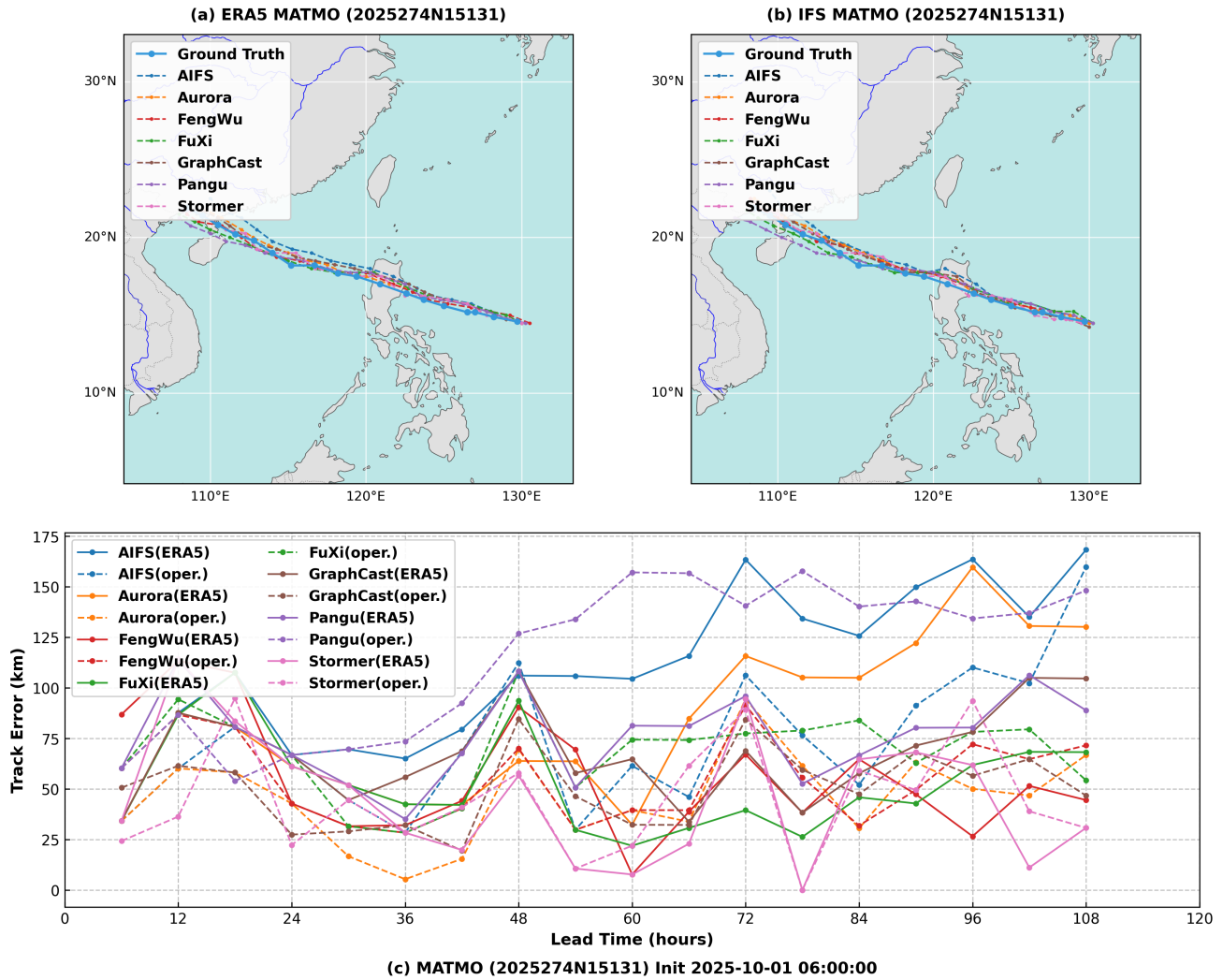


Figure 19. Track forecasts initialized from (a) ERA5 and (b) IFS analysis for Typhoon Matmo (IBTrACS ID 2025274N15131; initialization 0600 UTC 1 October 2025). Observed track from IBTrACS (blue). (c) Mean-distance track error versus lead time (0–120 h) for each model and initialization.

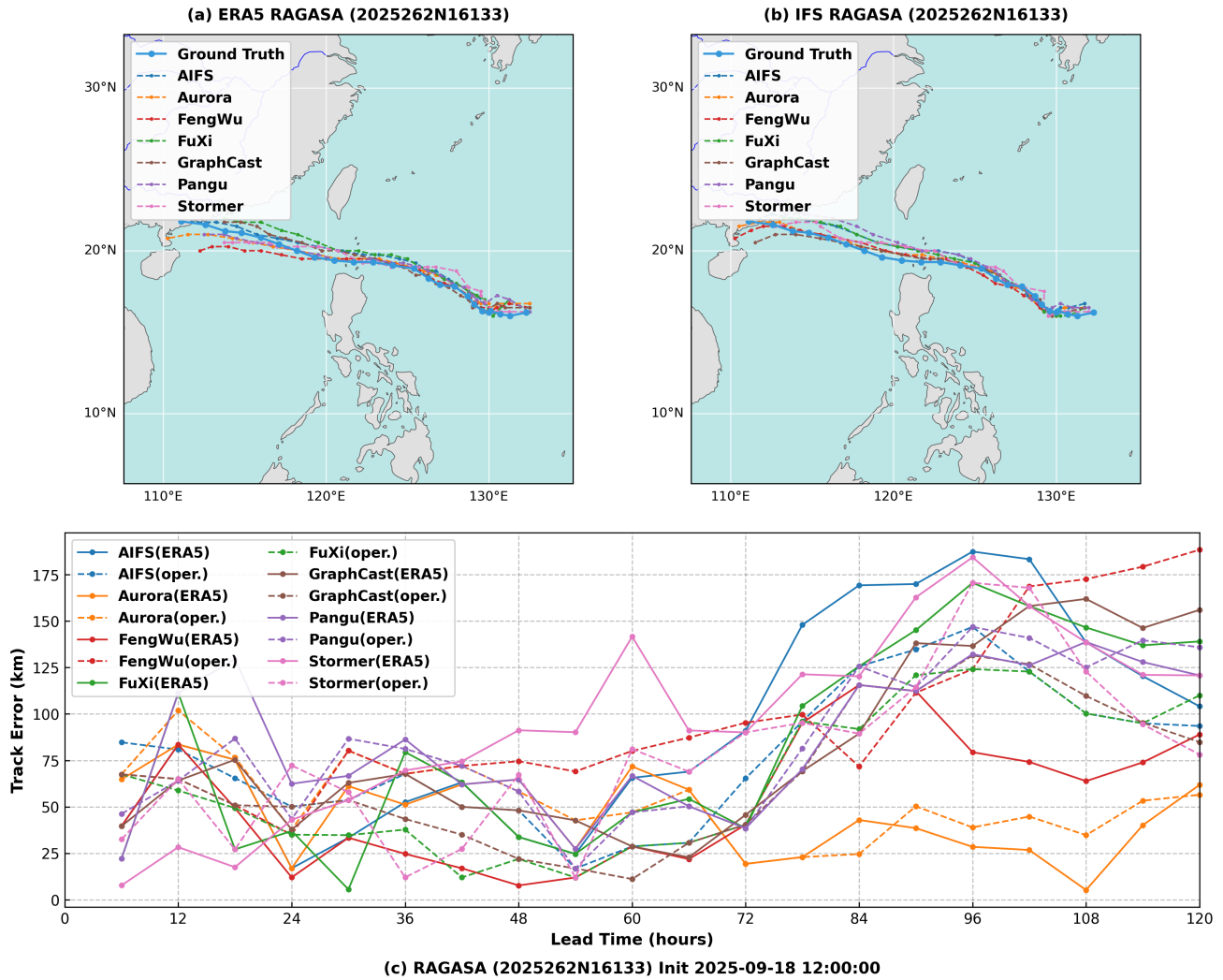


Figure 20. Track forecasts initialized from (a) ERA5 and (b) IFS analysis for Typhoon Ragasa (IBTrACS ID 2025262N16133; initialization 1200 UTC 18 September 2025). Observed track from IBTrACS (blue). (c) Mean-distance track error versus lead time (0–120 h) for each model and initialization.

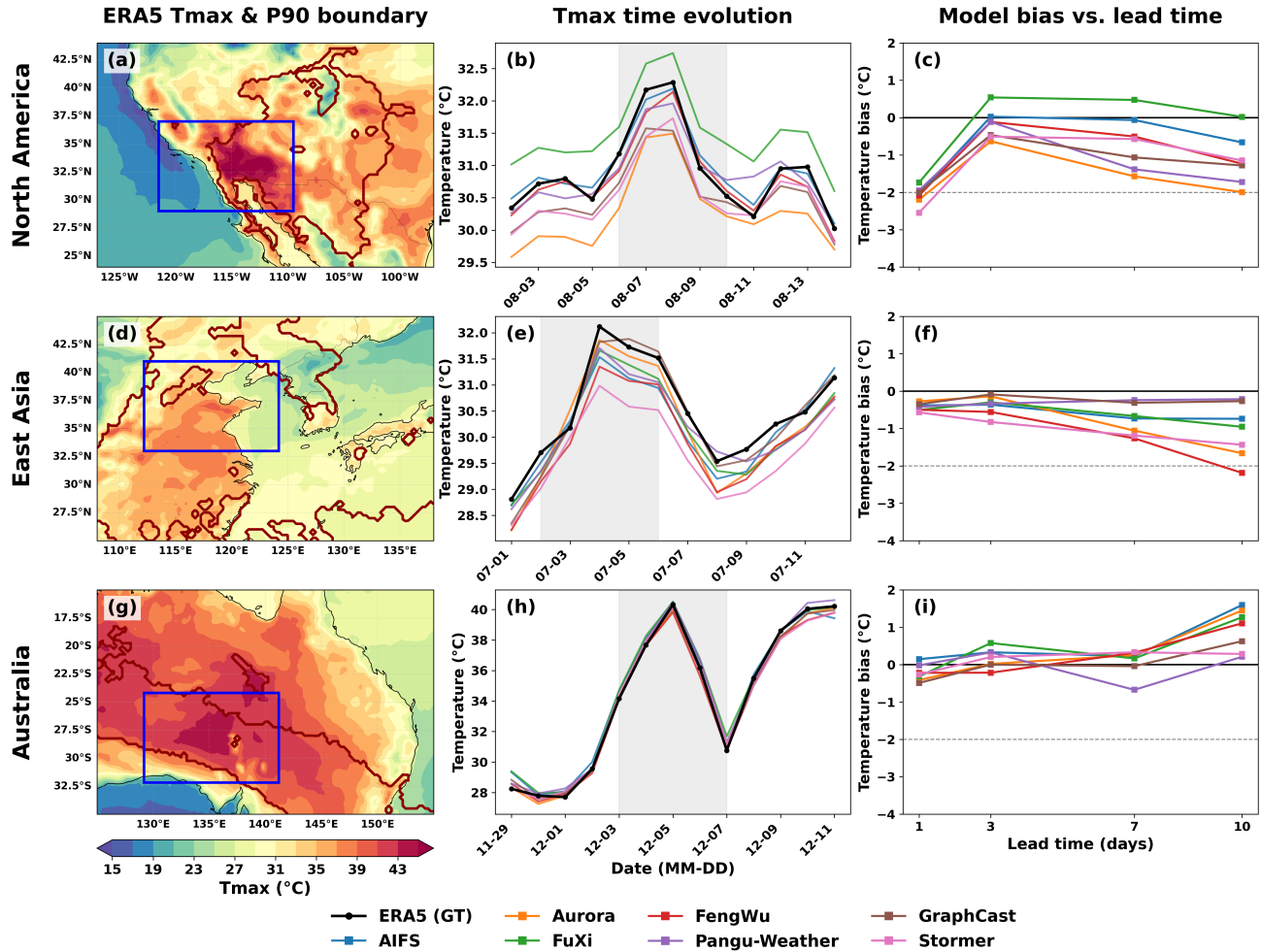


Figure 21. Multiple AI models for three major heatwave (HW) events in the second half of 2025: (a–c) North America; (d–f) East Asia; and (g–i) Australia. (a, d, and g) ERA5 daily maximum temperature (Tmax, shading, in °C) on the peak day of each event. Dark red contours denote the object-based HW boundaries (Tmax exceeding the local 90th percentile climatological threshold), and blue boxes indicate the regions for area-averaged analysis. (b, e, and h) Temporal evolution of the area-weighted Tmax over the blue boxes for ERA5 (black) and seven AI models at a 3-day forecast lead time. The core HW period is shaded in gray, with vertical dashed lines marking the peak day. (c, f, and i) Model bias in Tmax (°C) as a function of forecast lead time (1, 3, 7, and 10 days), averaged over the core HW period. Negative values at longer lead times reveal a systematic underestimation of extreme heat intensity.

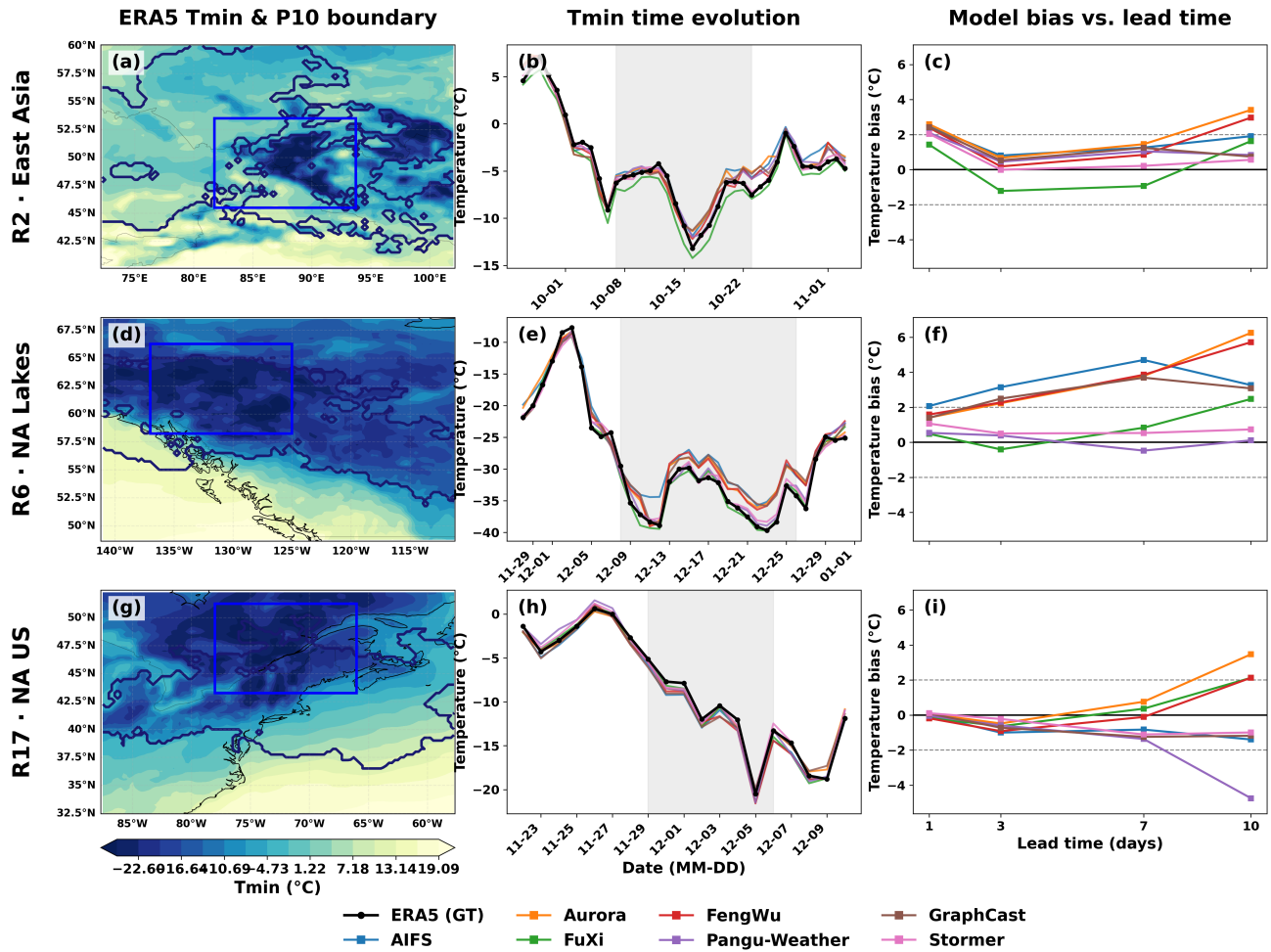


Figure 22. Multiple AI models for three major cold-surge (CS) events in the second half of 2025: (a–c) East Asia; (d–f) North America (Great Lakes); and (g–i) North America (CONUS). (a, d, and g) ERA5 daily minimum temperature (Tmin, shading, in °C) on the peak day of each event. Dark blue contours denote the object-based CS boundaries (Tmin below the local 10th percentile climatological threshold), and blue boxes indicate the regions for area-averaged analysis. (b, e, and h) Temporal evolution of the area-weighted Tmin over the blue boxes for ERA5 (black) and seven AI models at a 3-day forecast lead time. The core CS period is shaded in gray, with vertical dashed lines marking the peak day. (c, f, and i) Model bias in Tmin (°C) as a function of forecast lead time (1, 3, 7, and 10 days), averaged over the core CS period. Positive values at longer lead times indicate a systematic warm bias (underestimation of cold extremes).